

Solving and Learning Advective Multiscale Darcian Dynamics with the Neural Basis Method

Yuhe Wang* Min Wang†

Abstract

Physics-governed models are increasingly paired with machine learning for accelerated computations, yet most “physics-informed” formulations treat the governing equations as a penalty loss whose scale and meaning are set by heuristic balancing. This blurs operator structure, thereby confounding solution approximation error with governing-equation enforcement error and making the solving and learning progress hard to interpret and control. Here we introduce the Neural Basis Method, a projection-based formulation that couples a predefined, physics-conforming neural basis space with an operator-induced residual metric to obtain a well-conditioned deterministic minimization. Stability and reliability then hinge on this metric: the residual is not merely an optimization objective but a computable certificate tied to approximation and enforcement, remaining stable under basis enrichment and yielding reduced coordinates that are learnable across parametric instances. We use advective multiscale Darcian dynamics as an engineering demonstration to illustrate this broader point. Our method produces accurate and robust solutions in single solves and enables fast and effective parametric inference for essential engineering tasks such as control, optimization and uncertainty quantification.

Keywords: neural basis method, operator learning, parametric inference, reduced-order modeling, Darcy flow and transport, multiscale flow simulation

1. Introduction

Flow-transport coupling in multiscale porous materials [1, 2] poses major challenges for modeling, especially in parametric many-query workflows [3, 4]. Governed by elliptic-parabolic and advective PDEs with heterogeneous coefficients, such multiphysics dynamics entail conservation constraints, nonlinear effects, and multiscale interactions [5, 6]. Physics-informed machine learning [7], such as physics-informed neural networks (PINNs) [8, 9], is often presented as promising because it offers mesh-free approximations, seamless data integration, and potential learning-enabled acceleration. In practice, however, most approaches enforce physics through dimensionless L^2 loss minimization with heuristic weighting, which obscures physical scaling and disrupts numerical structure. This can yield poorly conditioned optimization in which approximation error is entangled with operator inconsistency, undermining accuracy and reliability [10–14]. This raises a fundamental question: where should physics and numerical structure reside in learning-based PDE models?

In this work, we propose the Neural Basis Method (NBM), which departs from loss-driven training by seeking solutions through an explicit, deterministic procedure. We use predefined physics-conforming neural networks to construct finite-dimensional approximation spaces. Then, we impose

*Asia Pacific Technology, Inc., Houston, TX 77042, USA; Institute for Scientific Computation, Texas A&M University, College Station, TX 77843, USA. yuhe.wang@me.com

†Department of Mathematics, University of Houston, Houston, TX 77204, USA. mwang55@central.uh.edu

PDEs by formulating a well-defined projection problem and solve for the solution coefficients. This design aligns NBM with classical numerical analysis and allows us to incorporate variational formulations [15] in a systematic and principled manner. Furthermore, for parametric cases, we represent solution families across parameter instances within the same neural space by learning the parameter-dependent solution coefficients, which naturally yields an operator learning formulation. This perspective is especially useful in many-query engineering settings under varying coefficients, boundary conditions, or control inputs.

NBM is motivated by two lines of ideas: projection-based methods (e.g., Galerkin), which use fixed finite-dimensional space to enable stability, error control, and systematic refinement [16, 17], and neural approximation approaches, which offer expressive spaces for representing solution manifolds [18–20]. NBM therefore aims to integrate neural representations while retaining the structure and guarantees of projection-based schemes. Related ideas have recently appeared, including random feature and extreme learning machine-type methods, where fixed single-hidden-layer neural networks serve as basis functions and solution coefficients are obtained by least-squares [21–28]. They provide an important proof-of-concept, but the non-orthogonal bases often yield severely ill-conditioned least-squares systems [29–32]. Especially, for multiscale problems, resolving fine-scale structures requires basis enrichment [22, 33–35], which can drive rapid, often exponential, condition-number growth. NBM builds on this direction while departing in three ways: a multilayer neural basis generator that resists conditioning degradation under basis enrichment; an essential physical structure that is built in at vector field representation level; and a weighting and stabilization strategy that enforces consistency with the underlying operator and physical scaling. Our design draws on insights from least-squares finite element methods (LSFEM) and the discontinuous Petro-Galerkin (DPG) framework. LSFEM inspires properly scaled boundary residuals in seeking solutions via operator-residual minimization [36–39]. DPG theory connects optimal test norms for multiscale and advective problems to generalized least-squares formulations [40, 41]. Collectively, these insights motivate the NBM view that weighting and stabilization are treated as principled components of the projection-based approach rather than as heuristic loss balancing, preserving operator consistency and physical scaling and enabling reliable residual-based measures.

A direct consequence of this projection-based perspective is that NBM provides a built-in, physically meaningful measure of solution quality. This stands in contrast to the penalty losses used in many physics-informed neural approaches, whose magnitude and minimization depend sensitively on heuristic balancing and offer limited insight into operator consistency. In NBM, the residual serves as a numerically interpretable certificate tied to the discrete PDE enforcement, supporting systematic reasoning about approximation error. Thus, residual reduction can be interpreted within a projection framework analogous to classical schemes, enabling stability analysis and error assessment in the spirit of Galerkin theory, including Céa-type approximation properties. This residual-based notion of measure underpins the reliability of both solution accuracy and subsequent parametric inference built on the learned representation.

We then extend NBM from single instance solves to parametric operator learning (NBM-OL). In many-query engineering tasks, including control, optimization, and uncertainty quantification, the goal is to learn how the solution operator varies with governing parameters [42–44]. This necessitates a measure that is numerically comparable across parameters and, under stable projection, provides a computable a posteriori bound on the solution error [45, 46]. In NBM-OL, we learn parametric dependence in the fixed neural basis space equipped with such measure, instead of surrogate losses that lack direct numerical meaning. This provides a robust utility for monitoring training and steering refinement across hyperparameters, with well-informed stopping criterion.

In this study, we present the first complete formulation and demonstration of NBM/NBM-OL in the setting of advective multiscale Darcian dynamics, with carbon storage as a representative application. We use physics-conforming neural vector bases in a nonlinear mixed Darcy flow formulation with energy-consistent weighting, and advance transport using a purely advective update stabilized by upwind control-volume treatment. As an introductory paper, we adopt a collocation-based realization for clarity and efficiency, although the method also supports variational formulations. Numerical experiments show accurate and stable single-instance solutions, and, for parametric inference, excellent in-distribution generalization, strong out-of-distribution robustness, and massive acceleration. In representative examples, we observe computational speedups on the order of 10^3 – 10^4 , and the gain scales with the prediction temporal horizon and problem size.

This paper is organized as follows. In the setting of coupled Darcy flow–transport, we first present the core ingredients of NBM and evaluate its performance on single-instance problems. We then turn to parametric many-query regimes, where variability arises from permeability fields and boundary conditions, and show how NBM-OL enables efficient parametric inference. Together, we illustrate the central principle of NBM: by placing physics in the neural discretization through physics-conforming approximation spaces and operator-induced residual metrics, the method unifies direct PDE solving and parametric operator learning within the same projection-based formulation.

2. Overview of NBM as a neural PDE solver

The overall workflow of NBM for coupled multiscale Darcy flow–transport (see Appendix A) is summarized in Fig. 1. It brings together the main components of the collocation-based implementation, including the underlying physical system, neural basis approximations for scalar (pressure, concentration) and vector fields (mass-flux), the mixed weighted least-squares formulation for the multiscale Darcy flow solution with energy-consistent weighting of interior and boundary residuals, and the implicit time-marching procedure for the coupled flow–transport dynamics.

2.1 Core NBM formulation

NBM approximates solutions with finite neural basis functions and computes the solution coefficients through a PDE-constrained least-squares projection. For system (A.1)-(A.2), the pressure $p(\mathbf{x}, t)$ and mass-flux $\mathbf{q}(\mathbf{x}, t)$ are smooth and therefore suit global basis expansion naturally. In contrast, the concentration $c(\mathbf{x}, t)$ can develop limited regularity with discontinuous fronts and thus requires specialized stabilization or regularization. In general, we write $s_{NN}(\mathbf{x}, t) = \sum \theta_i(t) \phi_i(\mathbf{x})$, where a multilayer, fixed-parameter, ResNet-style network [47] generates the scalar spatial bases $\{\phi_i(\mathbf{x})\}$. Moreover, we let the coefficient vector $\boldsymbol{\theta}(t)$ carry temporal evolution. Here s denotes a scalar field, namely pressure, concentration, or a mass-flux component such as q_x or q_y . We freeze network weights/biases, so we define a deterministic approximation space $\text{span}\{\phi_i\}$ and obtain the solution by projecting onto this space rather than by training the network. Specifically, we use two hidden layers to balance expressiveness and numerical conditioning while maintaining a clear geometric interpretation of the induced basis functions. We refer to this construction as a dual-layer neural basis.

For the vector field \mathbf{q} , we propose a neural basis design inspired by the Helmholtz decomposition [48, 49] such that we approximate via a sum of a divergence-free part $\phi_i^{(\text{div})}$ and curl-free part $\phi_i^{(\text{curl})}$,

$$\mathbf{q}_{NN} = \sum \left[\theta_i^{(\text{div})} \phi_i^{(\text{div})} + \theta_i^{(\text{curl})} \phi_i^{(\text{curl})} \right]. \quad (1)$$

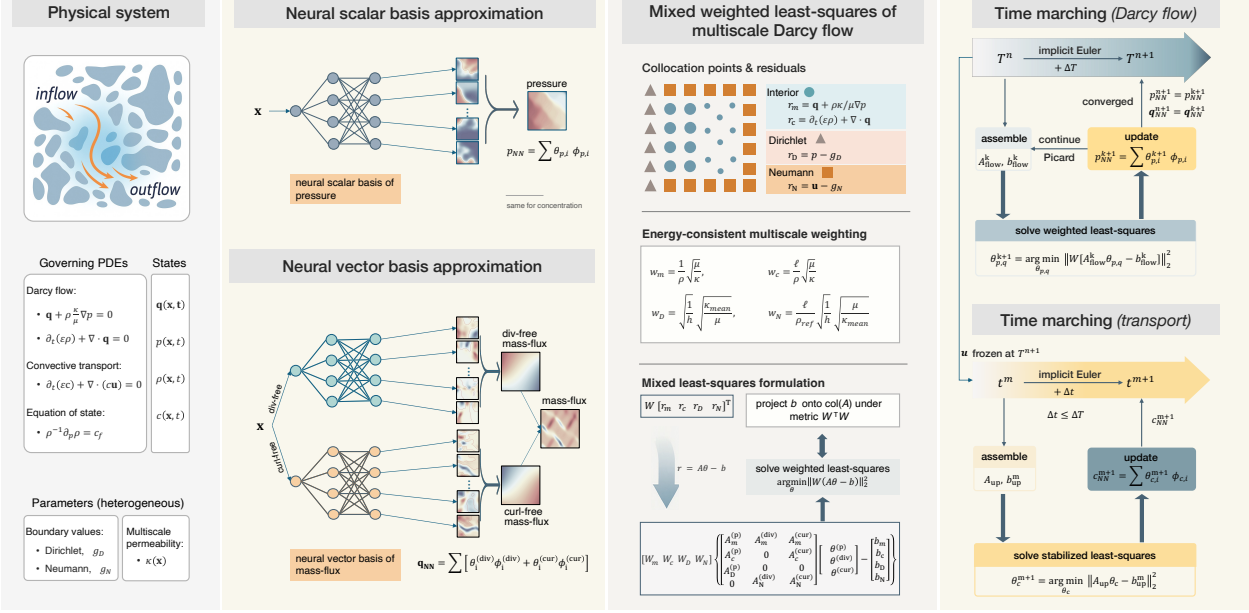


Fig. 1 | Overview of NBM as a neural PDE solver for coupled multiscale Darcy flow–transport. Left, Physical system. Middle-left, Neural basis approximation for scalar and vector field. Middle-right, Mixed weighted least-squares projection for multiscale Darcy flow. Right, Time marching of Darcy flow and transport.

We build the curl-free part as $\phi_i^{(\text{curl})} = \nabla \phi_i$, which represents the irrotational flow driven by potential. For the divergence-free part, we use a streamfunction formulation in 2D, $\phi_i^{(\text{div})} = \nabla^\perp \phi_i$, and a vector potential formulation in 3D, $\phi_i^{(\text{div})} = \nabla \times \mathbf{F}_i$, where \mathbf{F}_i can be constructed from the same scalar basis $\{\phi_i\}$. By this design, $\nabla \cdot \phi_i^{(\text{div})} = 0$ holds identically, so only the curl-free subspace enters equation (A.2); it supplies the degrees of freedom needed to represent compressible effects and source-driven mass redistribution, while the divergence-free component naturally captures mass-preserving motion. This physics-conforming representation preserves the intrinsic structure of fluid motion as much as possible at the representation level and can effectively improve solution accuracy. See Appendices B-E for details of construction and properties of neural basis functions.

To compute the coefficient vector θ at each time step or linearization iterate, NBM enforces (A.4) via minimizer $\theta^* = \arg \min_{\theta} \|\mathcal{L}[\sum \theta_i \phi_i]\|_{\Omega}^2 + \|\mathcal{B}[\sum \theta_i \phi_i] - g\|_{\partial\Omega}^2$, which is linear in $\{\theta_i\}$ with $\{\phi_i\}$ being fixed. After neural discretization, it becomes $\theta^* = \arg \min_{\theta} \|\mathbf{A}\theta - \mathbf{b}\|_{\mathbf{V}}^2$, where \mathbf{A} and \mathbf{b} encode the discretized PDE operators and boundary conditions under certain time stepping or linearization, and \mathbf{V} denote a properly-chosen norm in a general sense. In collocation-based realization we enforce the PDEs at collocation points. This minimization admits a projection interpretation: its residual is orthogonal to $\text{col}(\mathbf{A})$ under $\langle \cdot, \cdot \rangle_{\mathbf{V}}$, so we enforce the PDE constraints via a least-squares projection in the neural basis space. In practice, NBM removes nonconvex training altogether: at each update, θ is obtained by solving a deterministic linear or linearized least-squares system, retaining the operator structure of classical schemes. Furthermore, under standard continuity and stability assumptions, this projection admits a probabilistic Céa-type bound: the error is controlled by the best approximation in the N_b -dimensional neural basis space, plus a high-probability $N_b^{-1/2}$ term, which is a conservative baseline guarantee provided by the following theoretical analysis.

Lemma 1 (Probabilistic Céa-type bound for neural basis spaces). *Let V be a Hilbert space equipped with norm $\|\cdot\|_V$, and let $a(\cdot, \cdot) : V \times V \rightarrow \mathbb{R}$ be a continuous bilinear form with continuity constant $C_a > 0$ and stability constant $\gamma > 0$ (either coercive or inf-sup stable). Let $\{\phi_\omega\}_{\omega \sim \pi} \subset V$ denote*

a family of fixed neural basis functions parameterized by random variables ω drawn i.i.d. from a distribution π , and define the N_b -dimensional neural basis space

$$V_{N_b} := \text{span}\{\phi_{\omega_1}, \dots, \phi_{\omega_{N_b}}\} \subset V, \quad \omega_j \stackrel{\text{i.i.d.}}{\sim} \pi, \quad j = 1, \dots, N_b.$$

Let $u \in V$ be the exact solution of

$$a(u, v) = \ell(v), \quad \forall v \in V,$$

and let $u_{N_b} \in V_{N_b}$ denote the least-squares projection solution associated with the NBM formulation. Assume that u belongs to the reproducing kernel Hilbert space \mathcal{H}_k induced by the random neural basis construction, and that \mathcal{H}_k is continuously embedded in V ,

$$\|w\|_V \leq C_{\text{emb}} \|w\|_{\mathcal{H}_k}, \quad \forall w \in \mathcal{H}_k,$$

where C_{emb} is the embedding constant of $\mathcal{H}_k \hookrightarrow V$. Then, for any $\delta \in (0, 1)$, there exists a constant $C_1(\delta) > 0$ such that, with probability at least $1 - \delta$,

$$\|u - u_{N_b}\|_V \leq \frac{C_a}{\gamma} \left(\inf_{w \in \mathcal{H}_k} \|u - w\|_V + C_{\text{emb}} C_1(\delta) N_b^{-1/2} \right).$$

If, in addition, $u \in \mathcal{H}_k$ with $\|u\|_{\mathcal{H}_k} \leq B$, then

$$\|u - u_{N_b}\|_V \leq \frac{C_a}{\gamma} C_{\text{emb}} C_1(\delta) B N_b^{-1/2}.$$

Proof. By the Céa estimate associated with the Galerkin or least-squares projection, the NBM solution $u_{N_b} \in V_{N_b}$ satisfies

$$\|u - u_{N_b}\|_V \leq \frac{C_a}{\gamma} \inf_{w \in V_{N_b}} \|u - w\|_V. \quad (2)$$

Since $u \in \mathcal{H}_k$, classical results on Monte–Carlo approximation of kernel expansions (e.g., Rahimi–Recht or Bach-type bounds) imply that, for any $\delta \in (0, 1)$, with probability at least $1 - \delta$, there exists a function $v_{N_b} \in V_{N_b}$ such that

$$\|u - v_{N_b}\|_{\mathcal{H}_k} \leq C_1(\delta) \|u\|_{\mathcal{H}_k} N_b^{-1/2}. \quad (3)$$

Here v_{N_b} is a comparison function in V_{N_b} whose existence is guaranteed by random feature approximation theory and $C_1(\delta)$ is a constant depends on δ but is independent of N_b . Using the continuous embedding $\mathcal{H}_k \hookrightarrow V$, we obtain

$$\|u - v_{N_b}\|_V \leq C_{\text{emb}} \|u - v_{N_b}\|_{\mathcal{H}_k}. \quad (4)$$

Combining (3) and (4) yields

$$\|u - v_{N_b}\|_V \leq C_{\text{emb}} C_1(\delta) \|u\|_{\mathcal{H}_k} N_b^{-1/2}. \quad (5)$$

Since $v_{N_b} \in V_{N_b}$, by definition of the infimum,

$$\inf_{w \in V_{N_b}} \|u - w\|_V \leq \|u - v_{N_b}\|_V. \quad (6)$$

Substituting (6) into the Céa's estimate (2) and using (5) gives

$$\|u - u_{N_b}\|_V \leq \frac{C_a}{\gamma} C_{\text{emb}} C_1(\delta) \|u\|_{\mathcal{H}_k} N_b^{-1/2}.$$

More generally, without assuming a bound on $\|u\|_{\mathcal{H}_k}$, the same argument yields

$$\|u - u_{N_b}\|_V \leq \frac{C_a}{\gamma} \left(\inf_{w \in \mathcal{H}_k} \|u - w\|_V + C_{\text{emb}} C_1(\delta) N_b^{-1/2} \right).$$

□

The above bound does not rely on symmetry of the operator. For the transport equation, the bilinear form $a(\cdot, \cdot)$ is generally non-symmetric but satisfies an inf-sup condition under appropriate least-squares norms. In such cases, the constant γ represents the corresponding inf-sup stability constant. Since the NBM formulation employs a deterministic least-squares realization, which can be interpreted as a Petrov–Galerkin projection, the same Céa-type estimate applies.

2.2 Mixed least-squares with energy-consistent weights for multiscale Darcy flow

Discrete neural gradient and divergence operators are generally not adjoint. Consequently, a pressure-only approximation that eliminates \mathbf{q} through (A.1) and then recovers it a posteriori does not, in general, preserve local mass conservation when inserted into (A.2). We therefore devise a mixed formulation and solve $\boldsymbol{\theta}_p$ and $\boldsymbol{\theta}_q$ simultaneously using least-squares for each update by

$$\begin{aligned} \boldsymbol{\theta}_{p,q}^* = \arg \min_{\boldsymbol{\theta}_{p,q}} \left\{ \left\| \mathbf{q}_{NN} + \rho \frac{\kappa}{\mu} \nabla p_{NN} \right\|_{\Omega}^2 + \left\| \frac{\partial(\varepsilon \rho(p_{NN}))}{\partial t} + \nabla \cdot \mathbf{q}_{NN} \right\|_{\Omega}^2 \right. \\ \left. + \|p_{NN} - p_D\|_{\partial\Omega_p}^2 + \|\mathbf{q}_{NN} \cdot \mathbf{n} - q_N\|_{\partial\Omega_q}^2 \right\}. \end{aligned} \quad (7)$$

Here $\boldsymbol{\theta}_{p,q}$ denotes $(\boldsymbol{\theta}_p, \boldsymbol{\theta}_q)$, $p_{NN} = \sum_i \theta_{p,i} \phi_{p,i}$ and $\mathbf{q}_{NN} = \sum_i \theta_{q,i} \phi_{q,i}$, a compact form of (1). This mixed projection jointly enforces the constitutive law, the continuity constraint, and the boundary conditions, and produces locally conservative fluxes without a posterior correction. Additionally, $\|\cdot\|_{\Omega/\partial\Omega}$ denotes a generic norm defined in Ω or on $\partial\Omega$, and its construction hinges on how we measure the interior and boundary residuals.

Unweighted L^2 norms do not respect the Darcian energy scaling, which can degrade accuracy in multiscale media; this motivates energy-consistent weighting. Accordingly, we place all residual terms on a common Darcian energy scale: we weight the constitutive residual to match the dissipative metric $\int_{\Omega} \frac{\mu}{\kappa} |\mathbf{u}|^2 d\Omega$, and scale the continuity and boundary residuals to the same metric. Under collocation realization, this yields:

$$\begin{aligned} \boldsymbol{\theta}_{p,q}^* = \arg \min_{\boldsymbol{\theta}_{p,q}} \left\{ \left\| w_m \left(\mathbf{q}_{NN} + \rho \frac{\kappa}{\mu} \nabla p_{NN} \right) \right\|_{L^2(\Omega)}^2 + \left\| w_c \left(\frac{\partial(\varepsilon \rho(p_{NN}))}{\partial t} + \nabla \cdot \mathbf{q}_{NN} \right) \right\|_{L^2(\Omega)}^2 \right. \\ \left. + \|w_D (p_{NN} - p_D)\|_{L^2(\partial\Omega_p)}^2 + \|w_N (\mathbf{q}_{NN} \cdot \mathbf{n} - q_N)\|_{L^2(\partial\Omega_q)}^2 \right\}, \end{aligned} \quad (8)$$

with

$$w_m = \frac{1}{\rho} \sqrt{\frac{\mu}{\kappa}}, \quad w_c = \frac{\ell}{\rho} \sqrt{\frac{\mu}{\kappa_{\text{mean}}}}, \quad w_D = \sqrt{\frac{1}{h}} \sqrt{\frac{\kappa_{\text{mean}}}{\mu}}, \quad w_N = \frac{\ell}{\rho_0} \sqrt{\frac{1}{h}} \sqrt{\frac{\mu}{\kappa_{\text{mean}}}}. \quad (9)$$

In w_c and w_N , ℓ is a characteristic length that ensures dimensional consistency relative to the constitutive residual. The weights w_D and w_N balance the pressure and mass-flux boundary residuals against the interior energy scaling with a measure correction $\sqrt{1/h}$ to compensate for the codimension-one boundary sampling in collocation. Here h is the collocation spacing of the residual evaluation over the physical domain. κ_{mean} is the mean permeability and ρ_0 is the reference density. These weights measure all terms in compatible weighted L^2 norms and yield a consistent, physically interpretable projection.

In implementation, each residual evaluation at a collocation point corresponds to one row of the discrete weighted least-squares system. For interior points $x_i \in \Omega$ with associated volume $|\Omega_i|$, we use $w_m(x_j) = 1/\rho \sqrt{\mu/\kappa(x_j)} \sqrt{|\Omega_j|}$ for the constitutive residual and $w_c(x_j) = \ell/\rho \sqrt{\mu/\kappa_{\text{mean}}} \sqrt{|\Omega_j|}$ for the continuity residual. For boundary points $x_b \in \partial\Omega$ with associated length or area $|\partial\Omega_b|$, we set $w_D(x_b) = \sqrt{1/h} \sqrt{\kappa_{\text{mean}}/\mu} \sqrt{|\partial\Omega_b|}$ and $w_N(x_b) = \ell/\rho_{\text{ref}} \sqrt{1/h} \sqrt{\mu/\kappa_{\text{ref}}} \sqrt{|\partial\Omega_b|}$. Accordingly, the discrete residual vector takes the stacked form

$$\mathbf{r}(\boldsymbol{\theta}) = \begin{bmatrix} \mathbf{r}_m \\ \mathbf{r}_c \\ \mathbf{r}_D \\ \mathbf{r}_N \end{bmatrix} = \begin{bmatrix} \mathbf{A}_m \\ \mathbf{A}_c \\ \mathbf{A}_D \\ \mathbf{A}_N \end{bmatrix} \boldsymbol{\theta} - \begin{bmatrix} \mathbf{b}_m \\ \mathbf{b}_c \\ \mathbf{b}_D \\ \mathbf{b}_N \end{bmatrix}, \quad \boldsymbol{\theta} = \begin{bmatrix} \boldsymbol{\theta}^{(p)} \\ \boldsymbol{\theta}^{(\text{div})} \\ \boldsymbol{\theta}^{(\text{cur})} \end{bmatrix},$$

where $\mathbf{r}_m \in \mathbb{R}^{M_\Omega}$ and $\mathbf{r}_c \in \mathbb{R}^{M_\Omega}$ collect the constitutive and continuity residuals at interior collocation points, and $\mathbf{r}_D \in \mathbb{R}^{M_D}$ and $\mathbf{r}_N \in \mathbb{R}^{M_N}$ collect the Dirichlet and Neumann residuals at boundary collocation points. The corresponding discrete system has a block structure

$$\underbrace{\begin{bmatrix} \mathbf{A}_m^{(p)} & \mathbf{A}_m^{(\text{div})} & \mathbf{A}_m^{(\text{cur})} \\ \mathbf{A}_c^{(p)} & \mathbf{0} & \mathbf{A}_c^{(\text{cur})} \\ \mathbf{A}_D^{(p)} & \mathbf{0} & \mathbf{0} \\ \mathbf{0} & \mathbf{A}_N^{(\text{div})} & \mathbf{A}_N^{(\text{cur})} \end{bmatrix}}_{\mathbf{A}_{\text{flow}} \in \mathbb{R}^{M_{\text{tot}} \times N_\theta}} \begin{bmatrix} \boldsymbol{\theta}^{(p)} \\ \boldsymbol{\theta}^{(\text{div})} \\ \boldsymbol{\theta}^{(\text{cur})} \end{bmatrix} - \underbrace{\begin{bmatrix} \mathbf{b}_m \\ \mathbf{b}_c \\ \mathbf{b}_D \\ \mathbf{b}_N \end{bmatrix}}_{\mathbf{b}_{\text{flow}} \in \mathbb{R}^{M_{\text{tot}}}}, \quad M_{\text{tot}} = 2M_\Omega + M_D + M_N,$$

where each row of $\mathbf{A}_m, \mathbf{A}_c, \mathbf{A}_D, \mathbf{A}_N$ is obtained by evaluating the bases and their derivatives at the corresponding collocation point and inserting them into the constitutive, continuity, and boundary residual definitions. Finally, we have the following diagonal weighting matrix

$$\mathbf{W} = \text{diag}(\mathbf{w}_m, \mathbf{w}_c, \mathbf{w}_D, \mathbf{w}_N) \in \mathbb{R}^{M_{\text{tot}} \times M_{\text{tot}}},$$

where \mathbf{w}_m and \mathbf{w}_c collect the interior weights $w_m(x_j)$ and $w_c(x_j)$, while \mathbf{w}_D and \mathbf{w}_N collect the Dirichlet and Neumann boundary weights $w_D(x_b)$ and $w_N(x_b)$. We therefore write

$$\boldsymbol{\theta}_{p,q}^* = \arg \min_{\boldsymbol{\theta}_{p,q}} \|\mathbf{W}(\mathbf{A}_{\text{flow}} \boldsymbol{\theta}_{p,q} - \mathbf{b}_{\text{flow}})\|_2^2. \quad (10)$$

We then define a residual measure in a relative sense as $\mathcal{E}_{\text{rel}} = \|\mathbf{W}(\mathbf{A}_{\text{flow}} \boldsymbol{\theta}_{p,q} - \mathbf{b}_{\text{flow}})\|_2^2 / \|\mathbf{b}_{\text{flow}}\|_2^2$.

2.3 Upwind control-volume stabilization for transport

For transport, we treat the velocity field \mathbf{u}_{NN} as known and hold it frozen over each Darcy-flow update. To stabilize advection, we enforce (A.3) using a control-volume collocation with first-order upwinding. This gives the following discrete balance for each control-volume K

$$\varepsilon \frac{c_{NN,K}^{m+1} - c_{NN,K}^m}{\Delta t} |K| + \sum_{f \in \partial K} (\mathbf{u}_{NN} \cdot \mathbf{n})_f c_{NN,f}^{m+1, \text{up}} |f| = 0, \quad (11)$$

where $c_{NN} = \sum_i \theta_{c,i} \phi_{c,i}$, $|K|$ denotes the measure of the cell K , $|f|$ denotes the measure of a face $f \subset \partial K$, and m is the time index for transport update. The sign of $(\mathbf{u}_{NN} \cdot \mathbf{n})_f$ selects the upwind state and defines $c_{NN,f}^{m+1,\text{up}}$. We assemble each face flux by evaluating the neural basis $\phi_{c,i}$ in the upwind cell. The inflow boundary concentration then enters (11) naturally as the corresponding upwind state, eliminating explicit boundary residuals. This construction yields a linear least-squares solve for each concentration update. By inheriting the stability of classical upwinding finite-volume schemes while retaining a global low-dimensional neural representation, it effectively suppresses the spurious oscillations that global bases often introduce in advective regimes. Similarly, we write its compact form under collocation

$$\boldsymbol{\theta}_c^* = \arg \min_{\boldsymbol{\theta}_c} \|\mathbf{A}_{\text{up}} \boldsymbol{\theta}_c - \mathbf{b}_{\text{up}}\|_2^2, \quad (12)$$

where \mathbf{A}_{up} and \mathbf{b}_{up} are assembled by applying the upwind control-volume balance (11) to each cell and its residual measure is thus $\mathcal{E}_{\text{rel}} = \|\mathbf{A}_{\text{up}} \boldsymbol{\theta}_c - \mathbf{b}_{\text{up}}\|_2^2 / \|\mathbf{b}_{\text{up}}\|_2^2$. This construction defines an advection-aware residual metric and can be interpreted as an implicit, generalized weighting, analogous in spirit to the energy-consistent weighting used for Darcy flow.

2.4 Implicit time integration and nonlinearity treatment.

For Darcy flow, given p_{NN}^n at time T^n , we advance one Darcy time step ΔT to T^{n+1} by solving (10) with implicit time integration. For the nonlinearity induced by pressure-dependent density in (A.1), we choose Picard linearization. At Picard iterate k , we update the coefficients by

$$\boldsymbol{\theta}_{p,q}^{k+1} = \arg \min_{\boldsymbol{\theta}_{p,q}} \left\| \mathbf{W}(\mathbf{A}_{\text{flow}}^k \boldsymbol{\theta}_{p,q} - \mathbf{b}_{\text{flow}}^k) \right\|_2^2, \quad (13)$$

where $\mathbf{A}_{\text{flow}}^k$ and $\mathbf{b}_{\text{flow}}^k$ are evaluated using the previous iterate p_{NN}^k . With $p_{NN}^{k+1} = \sum \theta_{p,i}^{k+1} \phi_{p,i}$ and $\mathbf{q}_{NN}^{k+1} = \sum \theta_{q,i}^{k+1} \phi_{q,i}$, we iterate until convergence and obtain $(p_{NN}^{n+1}, \mathbf{q}_{NN}^{n+1})$ at T^{n+1} . At the end of each Darcy step, we then advance transport from T^n to T^{n+1} with frozen velocity $\mathbf{u}^{n+1} = \mathbf{q}_{NN}^{n+1} / \rho_{NN}^{n+1}$. We use implicit time integration to overcome CFL restriction. However, to better resolve the advective front propagation, we take multiple transport substeps within $[T^n, T^{n+1}]$ because concentration generally evolves on much smaller time scale than Darcy flow. Consequently, for each transport substep $t^m \rightarrow t^{m+1}$ in $[T^n, T^{n+1}]$, we formulate (12) as

$$\boldsymbol{\theta}_c^{m+1} = \arg \min_{\boldsymbol{\theta}_c} \|\mathbf{A}_{\text{up}} \boldsymbol{\theta}_c - \mathbf{b}_{\text{up}}^m\|_2^2, \quad (14)$$

where \mathbf{A}_{up} is fixed, while \mathbf{b}_{up}^m collects the previous-step result together with the boundary inflow condition. Then, when $t^{m+1} = T^{n+1}$, we set $c^{n+1} = c^{m+1} = \sum \theta_{c,i}^{m+1} \phi_{c,i}$.

3. Performance of NBM on single-query problems

In this section, we assess the performance of NBM on representative single-query Darcy–transport problems. We focus on solution accuracy, residual decay, basis refinement behavior, and robustness under increasing multiscale complexity. We begin with a homogeneous compressible benchmark to illustrate the basic approximation and convergence behavior of NBM, and then move to challenging multiscale permeability fields to examine the role of energy-consistent weighting and the robustness of the method in heterogeneous regimes.

3.1 NBM produces advective Darcian solutions with spectral-like accuracy

For a homogeneous compressible Darcy flow–transport problem based on supercritical CO₂ storage (Fig. 2a), the residual \mathcal{E}_{rel} decays in two near-linear stages on semi-log scale as the neural basis size N_b increases: a rapid drop that resolves dominant structures, followed by a milder slope as higher-frequency features become harder to represent with a finite basis (Fig. 2b). Consistent with this behavior, the relative L_2 errors of pressure, velocity, and concentration decrease rapidly and remain competitive with FVM across all variables (Fig. 2c). The velocity statistics also converge in a spectral-like manner, as quantified by the Kolmogorov–Smirnov distance, and the qualitative fields show systematic refinement with increasing N_b (Fig. 2d–e). For fieldwise errors in pressure, velocity, and concentration, we compare NBM against a finite-volume method (FVM) and a vanilla PINN. NBM attains a 0.001% relative L_2 error in pressure, about 50% lower than FVM (0.002%). For velocity, NBM yields 0.16% for u_x (FVM: 0.14%) and 0.30% for u_y (FVM: 0.33%), whereas the vanilla PINN underperforms (2.65% for u_x and 4.43% for u_y). For concentration, NBM (5.17%) closely matches FVM (5.36%), while the PINN degrades severely (100%) (Fig. 2f–i). The experiment details of this example are provided in Appendix F.

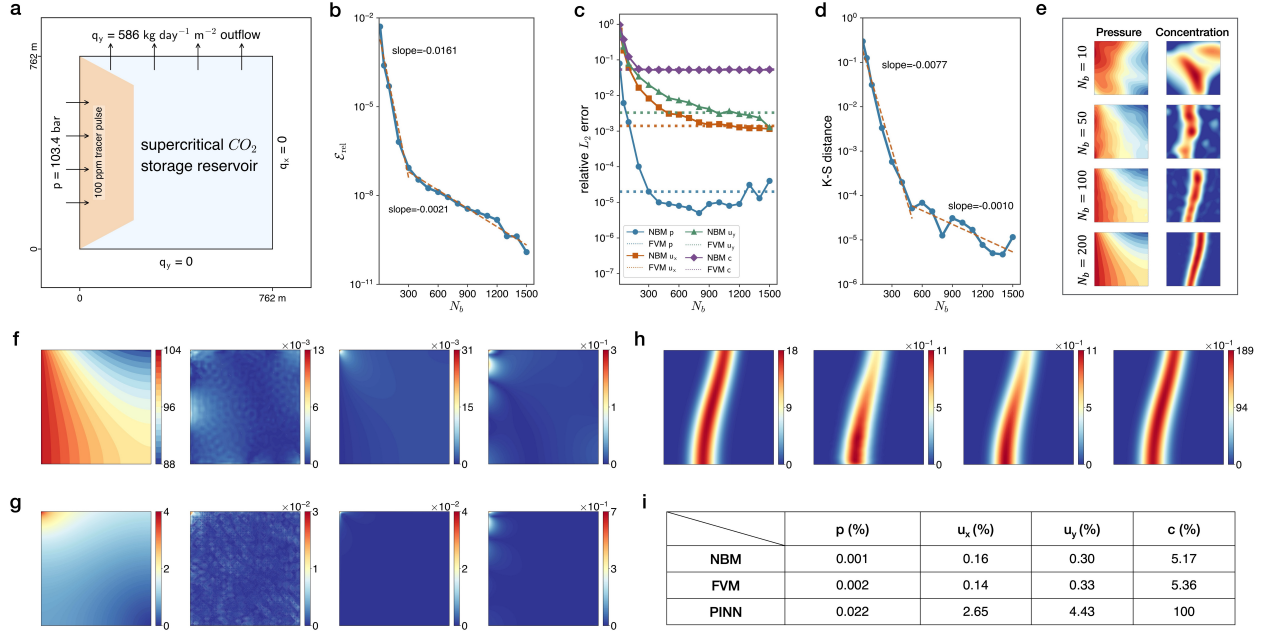


Fig. 2 | NBM performance on a homogeneous compressible benchmark. **a**, Homogeneous CO₂ storage model. **b**, Residual \mathcal{E}_{rel} vs. neural basis size N_b . **c**, Relative L_2 errors vs. N_b . **d**, Kolmogorov–Smirnov distance vs. N_b . **e**, Refinement of pressure and concentration solutions with N_b . **f**, Left to right: ground-truth pressure, followed by absolute error fields (w.r.t. ground truth) for NBM, FVM, and vanilla PINN. **g**, Left to right: ground-truth velocity magnitude, followed by absolute error fields (w.r.t. ground truth) for NBM, FVM, and vanilla PINN. **h**, Left to right: ground-truth concentration, followed by absolute error fields (w.r.t. ground truth) for NBM, FVM, and vanilla PINN. **i**, Relative L_2 errors. **Note:** All results are at 90 days. In f–i, NBM uses $N_b = 1000$, and all methods (NBM, FVM, and vanilla PINN) employ a 50×50 spatial resolution. Pressure is reported in bar, velocity in m day^{-1} , and concentration in ppm.

3.2 NBM remains accurate and robust for multiscale permeability fields

For this Darcy–transport problem but under a challenging multiscale permeability field (Fig. 3a), increasing the neural basis size N_b yields similar spectral-like residual decay together with systematic basis refinement (Fig. 3b–e). Using the FVM solution as a baseline, fieldwise comparisons show that energy-consistent weighting is critical in the multiscale regime: without weighting, the flow-

field energy-spectrum discrepancy $E(k)$ increases from 0.91% to 7.05% ($7.7\times$ increase), and the transport solution driven by this flow field deteriorates sharply, with the concentration relative L_2 difference rising from 4.09% to 17.6% ($4.3\times$) (Fig. 3f-j). By contrast, a vanilla PINN fails to produce meaningful solutions. Because a ground-truth is unavailable for this discrete-valued permeability field, the FVM solution is used only as a comparison baseline; discrepancies relative to it should not be interpreted as inaccuracy of NBM. We therefore include a manufactured-solution benchmark with a separable multiscale permeability to assess multiscale accuracy and robustness. NBM exhibits the same decay trend while converging to more accurate solutions than FVM (Fig. 3l-

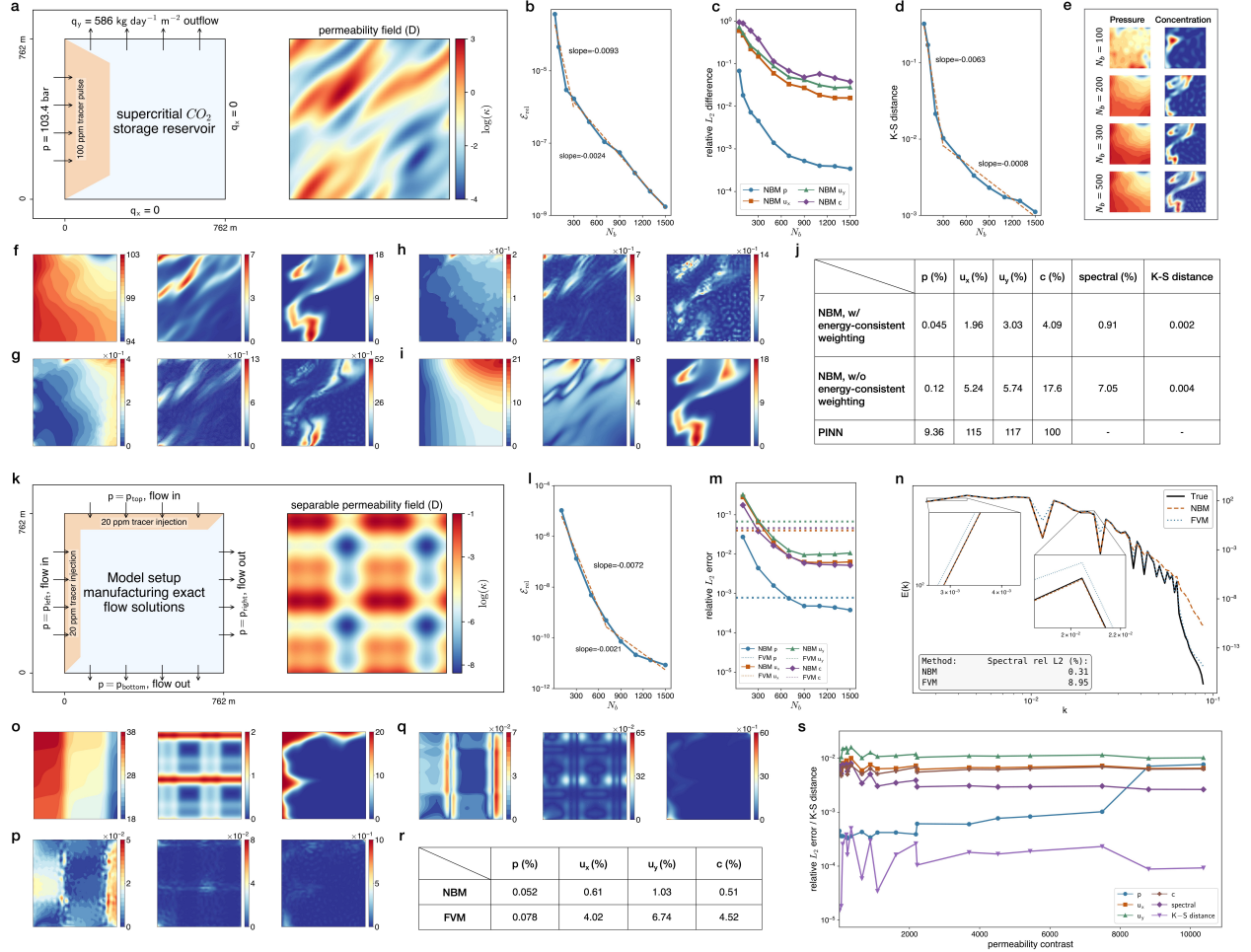


Fig. 3 | NBM performance on multiscale benchmarks. **a**, Multiscale CO₂ storage model. (permeability contrast 502). **b**, Residual \mathcal{E}_{rel} vs. neural basis size N_b . **c**, Relative L_2 difference vs. N_b . **d**, K-S distance vs. N_b . **e**, Refinement of NBM pressure and concentration fields with increasing N_b . **f**, Left to right: baseline pressure, velocity magnitude, and concentration. **g**, Left to right: absolute differences of NBM with energy-consistent weighting, for pressure, velocity magnitude, and concentration. **h**, Left to right: absolute differences of NBM without energy-consistent weighting, for pressure, velocity magnitude, and concentration. **i**, Left to right: absolute differences of PINN, for pressure, velocity magnitude, and concentration. **j**, Summary metrics measured against the baseline. **k**, Manufactured-solution setup (permeability contrast 1078). **l**, Residual \mathcal{E}_{rel} vs. N_b . **m**, Relative L_2 error vs. N_b . **n**, Energy spectrum $E(k)$ comparison. **o**, Ground-truth pressure, velocity magnitude, and concentration fields. **p**, Left to right: absolute errors of NBM, for pressure, velocity magnitude, concentration. **q**, Left to right: absolute errors of FVM, for pressure, velocity magnitude, concentration. **r**, Relative L_2 errors. **s**, Comparing metrics vs. permeability contrast. **Note:** Results in b-j are at 90 days. In f-j and o-s, NBM uses $N_b = 1000$, and all methods (NBM, FVM, and vanilla PINN) employ a 50×50 spatial resolution. Pressure is reported in bar, velocity in m day^{-1} , and concentration in ppm.

m), and the energy spectra confirm that it matches the dominant low-frequency mode of the true spectrum with much smaller spectral error (0.31% vs 8.95%) (Fig. 3n). NBM’s accuracy is also reflected in fieldwise errors: the relative L_2 errors drop from 0.078%/4.02%/6.74%/4.52% (FVM) to 0.052%/0.61%/1.03%/0.51% for (p, u_x, u_y, c) (Fig. 3o–r). Moreover, robustness to increasing permeability contrast is demonstrated up to 10^4 , with variable-wise and spectral relative L_2 errors and the K–S distance remaining controlled across the tested contrasts (Fig. 3s). The experiment details of this example are provided in Appendices F, G and I.

4. NBM operator learning for parametric Darcy flow–transport

The results above establish that NBM is accurate and robust, but single-instance NBM solver requires dense least-squares solutions. With N_b bases and M residual evaluations, the computational cost scales as $\mathcal{O}(MN_b^2)$, so NBM is not intended to compete with classical solvers in single-query settings. The situation changes in many-query regimes with parametric variations in PDE coefficients and boundary conditions, where repeated linear solves become the bottleneck in engineering design, control, and uncertainty analysis. NBM–OL addresses this by learning, offline, the parametric dependence of the solution coefficients in the predefined neural basis space and then evaluating them online at negligible cost.

We use NBM–OL to learn trajectory operators for the parametric system (A.5). Parametric encodings, together with time when relevant, are mapped to the neural basis coefficients, as summarized in Fig. 4. The parametric inputs include permeabilities $\boldsymbol{\xi}_\kappa$ and boundary values $\boldsymbol{\xi}_b$. To regularize learning and reduce dimensionality, we represent these inputs with low-dimensional encodings, as is standard in parametric PDE modeling [50]; for permeability, we use coarse blockwise parameters commonly adopted in geostatistical studies [51, 52]. The learned map predicts the neural basis coefficients, interpreted as the reduced coordinates of the solution in the NBM space. If additional compression is beneficial, we can apply proper orthogonal decomposition (POD) to the solution coefficient trajectories to further reduce the operator output dimension. The training process can be fully self-supervised, requiring no training data and thus avoiding dependence on expensive simulation databases. In addition, it minimizes the same residuals (13) and (14) used by the single-instance NBM solver for flow and transport. Notably, each residual provides an interpretable certificate for monitoring, diagnosis, and improving the learning process. Next, we first establish the respective equivalence relations with the solution errors using Lemmas 2 and 3 and then show that NBM–OL breaks the fundamental bottleneck of repeated parametric solves in many-query settings.

4.1 Residual–error certificate for the weighted Darcy projection

We consider a single implicit time step of the slightly-compressible Darcy update $T^n \rightarrow T^{n+1}$. The density increment satisfies $\rho(p^{n+1}) - \rho(p^n) = \rho_0 c_f (p^{n+1} - p^n)$. For clarity, here we show linearization by lagging the density prefactor at time level n and introduce $\alpha := \rho(p^n) \frac{\kappa}{\mu}$, $\beta := \frac{\varepsilon \rho_0 c_f}{\Delta T}$. Let (p, \mathbf{q}) denote the exact mixed state and $(\tilde{p}, \tilde{\mathbf{q}})$ its NBM approximation. The corresponding errors are $e_p = \tilde{p} - p$ and $e_{\mathbf{q}} = \tilde{\mathbf{q}} - \mathbf{q}$. We write (A.1)–(A.2) in the linearized time step-dependent form

$$\mathbf{q} + a \nabla p = 0 \quad \text{in } \Omega, \quad (15)$$

$$\nabla \cdot \mathbf{q} + \beta p = 0 \quad \text{in } \Omega, \quad (16)$$

with mixed boundary conditions $p = p_D$ on $\partial\Omega_p$ and $\mathbf{q} \cdot \mathbf{n} = q_N$ on $\partial\Omega_q$. We define the residuals

$$\begin{aligned} r_m &:= \tilde{\mathbf{q}} + a \nabla \tilde{p}, & r_c &:= \nabla \cdot \tilde{\mathbf{q}} + \beta \tilde{p}, \\ r_D &:= \tilde{p} - p_D, & r_N &:= \tilde{\mathbf{q}} \cdot \mathbf{n} - q_N. \end{aligned}$$

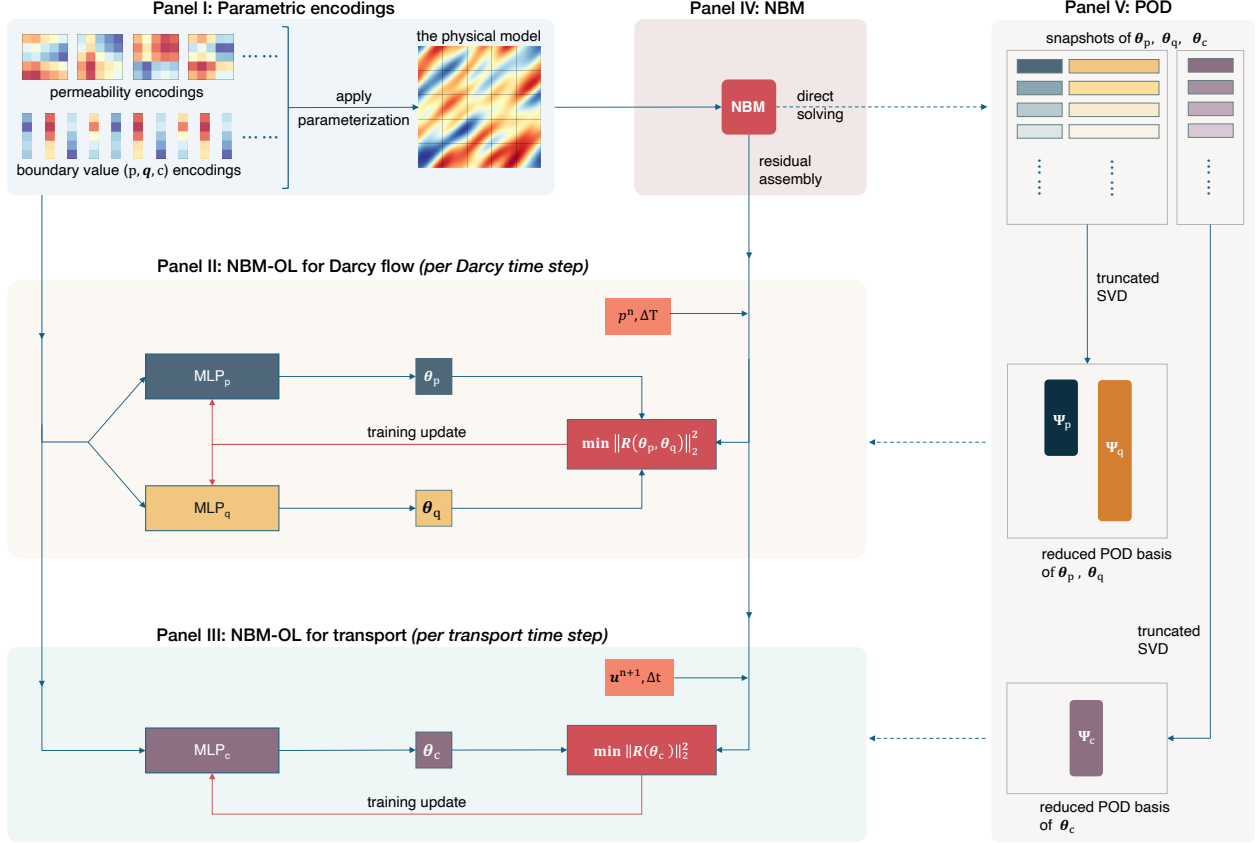


Fig. 4 | NBM-OL for parametric Darcy–transport systems. **Panel I**, Parameterization of permeability and boundary value. **Panel II**, NBM-OL for Darcy flow (per Darcy time step, ΔT). MLP_p and MLP_q learn the pressure and mass-flux solution coefficients θ_p and θ_q . Training is self-supervised by $\min \|\mathbf{R}(\theta_p, \theta_q)\|_2^2$ from (13), where $\mathbf{R}(\theta_p, \theta_q) = \mathbf{W}(\mathbf{A}_{\text{flow}} \theta_{p,q} - \mathbf{b}_{\text{flow}})$ with time stepping indices omitted. p^n denotes the pressure from the previous Darcy time-step, used for the current update. **Panel III**, NBM-OL for transport (per transport time-step, Δt). MLP_c learns concentration coefficients θ_c by $\min \|\mathbf{R}(\theta_c)\|_2^2$ from (14), where $\mathbf{R}(\theta_c) = \mathbf{A}_{\text{up}} \theta_c - \mathbf{b}_{\text{up}}$ with time stepping indices omitted. \mathbf{u}^{n+1} denotes the velocity after the current Darcy time-step update, computed as $\mathbf{u}^{n+1} = \mathbf{q}^{n+1}/\rho^{n+1}$. **Panel IV**, Optional POD compression of neural basis coefficients. Ψ_p , Ψ_q , and Ψ_c are the respective reduced POD bases.

and collect them in the weighted residual norm

$$\|R(\tilde{p}, \tilde{\mathbf{q}})\|_W^2 := \|w_m r_m\|_{L^2(\Omega)}^2 + \|w_c r_c\|_{L^2(\Omega)}^2 + \|w_D r_D\|_{L^2(\partial\Omega_p)}^2 + \|w_N r_N\|_{L^2(\partial\Omega_q)}^2,$$

where w_\star is given in (9) for $\star \in \{m, c, D, N\}$. We further write the natural graph norm of error

$$\|(e_p, e_{\mathbf{q}})\|_{\mathcal{E}}^2 := \|e_p\|_{H^1(\Omega)}^2 + \|e_{\mathbf{q}}\|_{H(\text{div}; \Omega)}^2 + \|e_p\|_{L^2(\partial\Omega_p)}^2 + \|e_{\mathbf{q}}\|_{L^2(\partial\Omega_q)}^2.$$

Then, Lemma 2 shows that this weighted residual norm is equivalent to the natural graph norm such that $\|R(\tilde{p}, \tilde{\mathbf{q}})\|_W \asymp \|(e_p, e_{\mathbf{q}})\|_{\mathcal{E}}$. Consequently, we provide a computable residual–error certificate.

Lemma 2 (Residual–error equivalence for the weighted first-order least-squares Darcy problem). *Assume $0 < a_{\min} \leq a(x) \leq a_{\max}$ and $0 < \beta_{\min} \leq \beta(x) \leq \beta_{\max}$ a.e. in Ω . Assume the boundary split $\partial\Omega = \partial\Omega_p \cup \partial\Omega_q$ ensures uniqueness, e.g., $|\partial\Omega_p| > 0$. Then there exist constants $C_1, C_2 > 0$, independent of $(\tilde{p}, \tilde{\mathbf{q}})$, such that*

$$C_1 \|(e_p, e_{\mathbf{q}})\|_{\mathcal{E}} \leq \|R(\tilde{p}, \tilde{\mathbf{q}})\|_W \leq C_2 \|(e_p, e_{\mathbf{q}})\|_{\mathcal{E}}, \quad (17)$$

Proof. The equivalence between $\|\cdot\|_W$ and the corresponding unweighted L^2 -residual norm follows from $0 < c_\star \leq w_\star \leq C_\star$. The error–residual equivalence (17) is the U -ellipticity result for the first-order system least-squares operator associated with (15)–(16); see, e.g., [38, 53]. \square

4.2 Residual–error certificate for the stabilized transport projection

We next consider an implicit transport sub-timestep $t^m \rightarrow t^{m+1}$ based on the upwind control-volume balance in (11). Let c denote the exact concentration and \tilde{c} its NBM approximation, and define the error by $e_c := \tilde{c} - c$. We further define the residual for this sub-timestep as $r_{\text{up}} := A_{\text{up}}\tilde{c} - b$, so that $r_{\text{up}} = A_{\text{up}}e_c$. For an arbitrary cellwise scalar field $v = \{v_K\}$, we introduce the pore-volume scaled diagonal mass weight $D := \text{diag}(\varepsilon|K|)$, $\|v\|_D^2 := \sum_K(\varepsilon|K|)v_K^2$. For each interior face $f = K|L$, let $\mathbf{n}_{K,f}$ denote the unit normal on f pointing outward from cell K , and set $\alpha_f := |(\mathbf{u} \cdot \mathbf{n}_{K,f})_f| |f|$. We can write the upwind dissipation semi-norm as $|v|_{\text{up}}^2 := \frac{1}{2} \sum_{f=K|L} \alpha_f (v_K - v_L)^2$. We then define the transport energy norm $\|v\|_{\mathcal{E},\text{tr}}^2 := \frac{1}{\Delta t} \|v\|_D^2 + |v|_{\text{up}}^2$. Since $|v|_{\text{up}}^2 \geq 0$, the transport energy norm controls the cellwise Euclidean error of concentration

$$\|e_c\|_2 \leq \sqrt{\frac{\Delta t}{\varepsilon|K|_{\min}}} \|e_c\|_{\mathcal{E},\text{tr}}, \quad |K|_{\min} := \min_K |K|.$$

On a fixed discretization, $\|\cdot\|_{\mathcal{E},\text{tr}}$ and $\|\cdot\|_2$ are equivalent up to constants. The next lemma shows that the Euclidean residual norm $\|r_{\text{up}}\|_2$ is equivalent to the transport energy norm of the error, i.e., $\|r_{\text{up}}\|_2 \asymp \|e_c\|_{\mathcal{E},\text{tr}}$, thereby providing a computable residual–error certificate.

Lemma 3 (Residual–error equivalence for upwind control-volume transport problem). *Assume $\varepsilon > 0$ and a fixed transport discretization (mesh, velocity field, and time step). Then there exist constants $C_1, C_2 > 0$, independent of \tilde{c} , such that*

$$C_1 \|e_c\|_{\mathcal{E},\text{tr}} \leq \|r_{\text{up}}\|_2 \leq C_2 \|e_c\|_{\mathcal{E},\text{tr}}. \quad (18)$$

Proof. For the upwind control-volume operator $A = \frac{1}{\Delta t}D + V$, the symmetric part $V_s = \frac{1}{2}(V + V^\top)$ induces the classical upwind jump dissipation, i.e., $v^\top V_s v = |v|_{\text{up}}^2 \geq 0$ for all cell vectors v ; see, e.g., [54, 55]. Hence $G := \frac{1}{\Delta t}D + V_s \succ 0$ and $\|v\|_{\mathcal{E},\text{tr}}^2 = v^\top G v$. Writing $A = G + V_k$ with skew-symmetric $T_k = \frac{1}{2}(V - V^\top)$, the DPG theory yields the residual–error equivalence in the induced dual norm, $\|e\|_G \asymp \|Ae\|_{G^{-1}}$; see, e.g., [40, 41, 56]. Finally, on a fixed discretization, the Euclidean residual $\|r\|_2$ is equivalent to $\|r\|_{G^{-1}}$ by standard spectral norm equivalence for symmetric positive definite matrices, which completes (18). \square

4.3 Parametric Darcy flow under varying permeability and boundary flux

We here assess whether NBM–OL can learn the Darcy flow operator under two different types of parametric variation: distributed permeability uncertainty and scalar boundary-flux control. Case-I considers an incompressible setting in which the base permeability field is parameterized through a piecewise-constant 5×5 coarse-block representation (block25), yielding a reduced operator family that retains the dominant spatial variability. Case-II considers the multiscale CO₂ storage model, where the varying parameter is the uniform top-boundary mass flux in [488, 976] kg/(m² day). Together, these two cases probe whether NBM–OL can handle both field variation and control variation (Fig. 5).

For Case-I, NBM–OL achieves consistently low in-distribution relative L_2 errors for pressure and velocity (Fig. 5e). More importantly, the learned operator remains robust under out-of-distribution

shifts in heterogeneity level, correlation length, and spatial rotation (Fig. 5f–h), indicating that the model captures structural flow responses rather than narrowly interpolating within the training ensemble. For Case-II, the learned operator again produces tightly clustered sub-percent errors in-distribution (Fig. 5l). Its accuracy is further preserved when extrapolating the boundary-flux magnitude by 50% beyond the training range and when extending the prediction horizon by 100% (Fig. 5m–n), demonstrating stable parametric and temporal generalization in the transient setting.

The training diagnostics show a clean decay of the normalized residual and, more importantly, a near-linear relation between $\sqrt{\mathcal{E}_{\text{rel}}}$ and the solution L_2 errors across test cases; see Fig. 5o. This identifies $\sqrt{\mathcal{E}_{\text{rel}}}$ as a practically useful accuracy indicator during learning, unlike generic optimization losses that need not reflect state accuracy in operator learning. As expected, NBM-OL supports rapid repeated parametric evaluation, delivering orders-of-magnitude speedups over FVM (Fig. 5q). The experiment setups and implementation details are provided in Appendix H.

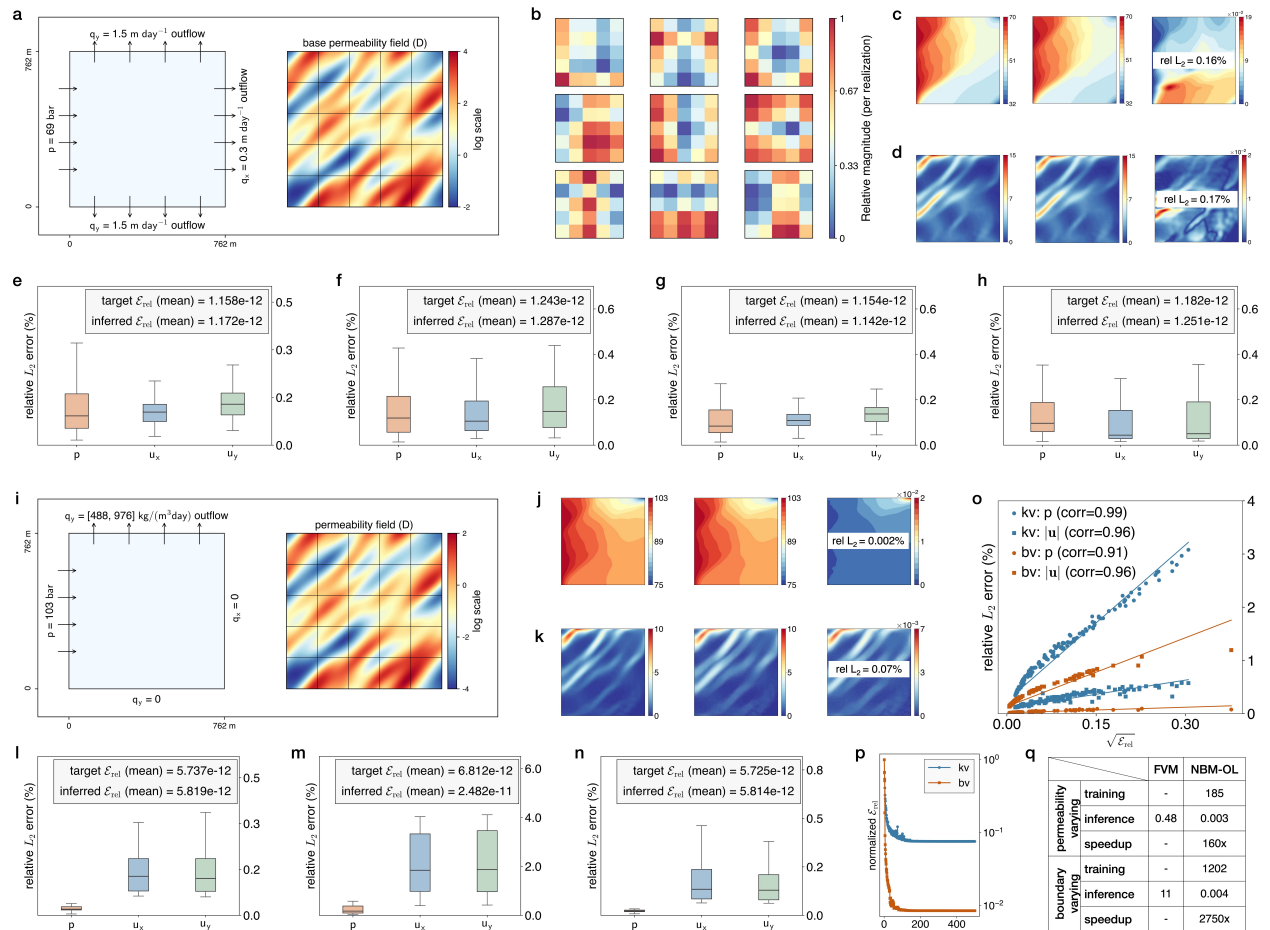


Fig. 5 | NBM-OL learns parametric Darcy flow operators under varying permeability and boundary flux. **a**, Problem setup (kv) and base permeability field. **b**, Representative block25 parametrizations. **c-d**, Left to right: true pressure/velocity magnitude, predicted pressure/velocity magnitude, respective absolute error fields. **e**, In-distribution generalization. **f-h**, Out-of-distribution generalization across heterogeneity level, correlation length, and spatial rotation. **i**, Problem setup (bv) and permeability field. **j-k**, Left to right: true pressure/velocity magnitude, predicted pressure/velocity magnitude, respective absolute error fields, at 200 days. **l**, In-distribution generalization. **m**, Out-of-distribution generalization in boundary flux. **n**, Out-of-distribution generalization in time horizon. **o**, Residual-error correlation during training: $\sqrt{\mathcal{E}_{\text{rel}}}$ vs. relative L_2 errors. **p**, Training dynamics measured by normalized \mathcal{E}_{rel} . **q**, Runtime comparison and speedups of NBM-OL relative to FVM, reported as CPU wall-time statistics in seconds. **Note**: Pressure is reported in bar and velocity in m day^{-1} .

4.4 Parametric Darcy–transport under coupled flow and transport dynamics

In Fig. 6, we consider a more stringent task in which transport is coupled with Darcy flow. The transport component introduces sharper, hyperbolic solution features, so accurate prediction of evolving concentration fronts becomes a harder test for reduced operator representations. In this setting, both the boundary mass-flux and the injected tracer concentration are treated as parameters within the same multiscale CO₂ storage configuration introduced earlier.

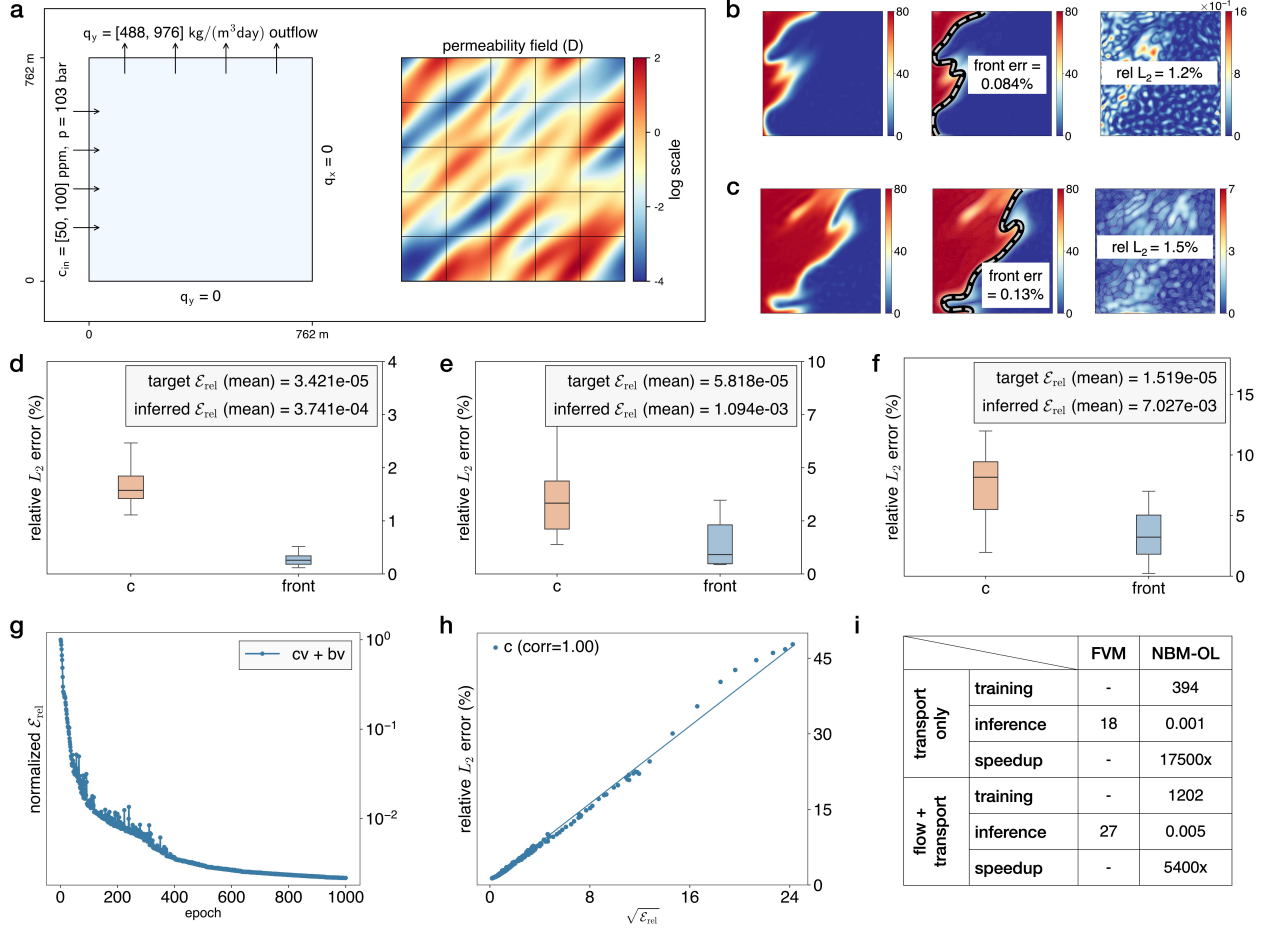


Fig. 6 | NBM-OL learns parametric Darcy–transport operators under varying boundary flux and concentration. **a**, Problem setup for boundary-flux-varying (bv) and injection-concentration-varying (cv) Darcy–transport operator learning. **b–c**, Left to right: true concentration, predicted concentration with the tracer front overlaid, and the corresponding absolute error; b is at 20 days and c is at 200 days. **d**, In-distribution generalization, measured by relative L_2 errors at 200 days over 100 random tests. **e**, Out-of-distribution generalization in boundary flux and concentration, measured by relative L_2 errors at 200 days over 100 random runs. **f**, Out-of-distribution generalization in time horizon, measured by relative L_2 errors at 400 days over 100 random runs. **g**, Training dynamics measured by normalized \mathcal{E}_{rel} . **h**, Residual-error correlation during training: $\sqrt{\mathcal{E}_{rel}}$ vs. relative L_2 errors. **i**, Runtime comparison and speedups of NBM-OL relative to FVM, reported as CPU wall-time statistics in seconds over 100 random runs. **Note:** Concentration is reported in ppm.

As shown in Fig. 6b–c, NBM-OL accurately predicts the concentration fields while preserving the location and shape of the evolving tracer fronts. When the boundary flux and injected concentration are sampled within the training ranges, the resulting in-distribution errors remain tightly clustered at very low levels; see Fig. 6d. More importantly, when both parameter ranges are extrapolated by 50% and the prediction horizon is extended by 100%, the error increase remains moderate and

no instability or catastrophic degradation is observed (Fig. 6e–f). This indicates that the learned operator captures the coupled flow–transport structure and front evolution mechanisms, rather than merely interpolating within the training ensemble.

Figures 6g–h further show that this residual-based accuracy indicator remains effective in the coupled flow–transport setting. Even with sharper transport dynamics, $\sqrt{\mathcal{E}_{\text{rel}}}$ continues to track concentration errors closely during training, indicating that the residual–error relation established for Darcy flow alone carries over to the more demanding coupled problem. Similarly, we achieve orders-of-magnitude speedups over FVM for parametric rollout using NBM–OL (Fig. 6i). See Appendix H for experiment setups and implementation details.

5. Conclusion

NBM is a general, projection-based neural framework that unifies solving and learning PDE-based systems. Its central idea is to move physics out of heuristic loss-driven training and into the neural discretization itself through physics-conforming approximation spaces and operator-induced residual metrics. It yields a well-conditioned deterministic minimization, in which the resulting residual is a numerically meaningful certificate tied to both solution approximation and PDE enforcement. This gives stability under basis enrichment, supports systematic accuracy assessment, and produces reduced coordinates as natural targets for parametric learning. These coordinates can be learned consistently across parameter instances, while the residual certificate remains an interpretable measure for monitoring, diagnosis, and improving operator predictivity. Beyond the Darcy–transport instantiation, the new method applies whenever a PDE admits stable discrete enforcement under an appropriate residual norm. Although we experiment rather simplified parameterizations, NBM–OL naturally extends to general parametric variations in operator coefficients, boundary conditions, and source terms, including spatially-varying and time-dependent profiles. From an engineering perspective, this makes the framework particularly attractive for repeated-query modeling under varying material properties, boundary conditions, and operating controls.

There are several directions to further broaden robustness and generality. Our current neural bases are global and can struggle with localized non-smoothness or nonconvex geometries, where Gibbs-type artifacts [57] may cause loss of accuracy. NBM, however, is not limited to global representations and can be localized via domain decomposition, partition-of-unity, or spectral-element-style [58] global–local hybrids. The presented weighting and stabilization are based on collocation and should be viewed as a simplified, not optimal, choice. More rigorous variational constructions can draw on DPG-inspired designs. Within this umbrella, we can further benefit from residual localization via Riesz representers [59], yielding a computable error indicator that drives adaptive enrichment where additional attention is needed. In this way, NBM can further provide a diagnostic tool that guides modeling design. Measurements can also be appended as additional residual blocks to uncover system parameters, informed by model-data identifiability and compatibility. Finally, NBM is not intended to circumvent the curse-of-dimensionality in high-dimensional PDEs, where the number of basis functions can become impractical. Most PDEs in science and engineering, however, are posed on 1D–3D spatial domains, which is the regime NBM targets. Extending to fully 3D systems is thus another natural step, where scalable residual evaluation, randomized least-squares, and effective preconditioning warrant further study.

Appendix A: Coupled Darcy flow–transport

We consider an isothermal compressible fluid flow through a two-dimensional heterogeneous porous continuum. The fluid motion is described by Darcy’s law and coupled with mass conservation:

$$\mathbf{q} + \rho \frac{\kappa}{\mu} \nabla p = 0, \quad (\text{A.1})$$

$$\frac{\partial(\varepsilon\rho)}{\partial t} + \nabla \cdot \mathbf{q} = 0, \quad (\text{A.2})$$

where $\mathbf{q}(\mathbf{x}, t)$ denotes the mass-flux, $p(\mathbf{x}, t)$ is the pressure, $\varepsilon(\mathbf{x})$ is the porosity, and $\rho(p)$ is the density, which is expressed through an equation of state, $\rho(p) = \rho_0(1 + c_f(p - p_0))$. c_f is the fluid compressibility and ρ_0 is the reference density at reference pressure p_0 . The viscosity μ and porosity ε are assumed constant, while $\kappa(\mathbf{x})$ is a spatially varying permeability field reflecting the heterogeneity of the medium. The Darcy velocity is $\mathbf{u} = \mathbf{q}/\rho$. In addition, we consider a passive scalar field $c(\mathbf{x}, t)$ representing a transported concentration, which evolves according to

$$\frac{\partial(\varepsilon c)}{\partial t} + \nabla \cdot (c \mathbf{u}) = 0, \quad (\text{A.3})$$

and is assumed not to influence the flow field. For clarity, source terms are omitted. With appropriate boundary conditions, equations (A.1)–(A.3) define a coupled Darcy flow–transport system that can be solved sequentially. Here, we use a standard finite-volume discretization to generate reference solutions, employing backward Euler time integration and first-order upwinding scheme for advection. In a compact form, we can express this dynamics as

$$\begin{aligned} \mathcal{L}(s(\mathbf{x}, t)) &= 0 \quad \text{in } \Omega, \\ \mathcal{B}(s(\mathbf{x}, t)) &= g \quad \text{on } \partial\Omega, \end{aligned} \quad (\text{A.4})$$

where $s(\mathbf{x}, t)$ denotes the collection of components from the primary unknowns, namely the pressure p , the mass-flux q , and the concentration c . In addition to single-instance solving, we consider a parametric family of problems in which the governing operators depend on parameters. Specifically, we distinguish between parameters associated with the interior operator in terms of operator coefficients and those associated with the boundary operator,

$$\mathcal{L}_{\boldsymbol{\xi}_\kappa}(s(\mathbf{x}, t)) = 0 \quad \text{in } \Omega, \quad \mathcal{B}_{\boldsymbol{\xi}_b}(s(\mathbf{x}, t)) = g_{\boldsymbol{\xi}_b} \quad \text{on } \partial\Omega, \quad (\text{A.5})$$

where $\boldsymbol{\xi}_\kappa$ parameterizes the spatial variations in the permeability field and $\boldsymbol{\xi}_b$ parameterizes the variations in boundary values. We collectively denote the full parameter vector by $\boldsymbol{\xi} = (\boldsymbol{\xi}_\kappa, \boldsymbol{\xi}_b)$. Equation (A.5) defines a family of PDE systems sharing a common structure for NBM-powered operator learning.

Appendix B: Neural basis construction and evaluation

Neural basis definition. Let $X \in \mathbb{R}^{M \times d}$ collect M prescribed spatial points in a d -dimensional domain, with each row giving one point. We build the neural basis by passing X through a fixed-parameter residual network with L layers and widths $\{p_1, \dots, p_L\}$, with $p_0 = d$. For $\ell = 0, 1, \dots, L$, let $A_\ell(X) \in \mathbb{R}^{M \times p_\ell}$ denote the layer- ℓ outputs evaluated at X , where rows correspond to spatial

points and columns to basis functions. For $\ell = 1, \dots, L$, we define

$$\begin{aligned} t_\ell(X) &= A_{\ell-1}(X) W_\ell^T + \mathbf{1} b_\ell^T, & a_\ell(X) &= t_\ell(X) \odot \alpha_\ell^T, \\ z_\ell(X) &= \sigma(a_\ell(X)), & s_\ell(X) &= \beta_\ell A_{\ell-1}(X) P_\ell^T, \\ A_\ell(X) &= s_\ell(X) + z_\ell(X), \end{aligned}$$

where $W_\ell, P_\ell \in \mathbb{R}^{p_\ell \times p_{\ell-1}}$, $b_\ell \in \mathbb{R}^{p_\ell}$, $\alpha_\ell \in \mathbb{R}^{p_\ell}$, and $\beta_\ell \in \mathbb{R}$. Here $\mathbf{1} \in \mathbb{R}^M$ is the all-ones vector, \odot denotes elementwise multiplication with broadcasting, and σ acts elementwise. Here, $\sigma(\cdot)$ is taken as $\tanh(\cdot)$. The columns of $A_L(X)$ define the neural basis at the M spatial points. When needed, the basis can be enriched by concatenating selected intermediate-layer outputs with $A_L(X)$.

Layer concatenation and constant basis. The neural basis in NBM need not be taken from a single layer. Given a user-specified index set $\mathcal{I} = \{i_1, \dots, i_K\}$ with $0 \leq i_k \leq L$, we define

$$\Phi(X) = [A_{i_1}(X) \ A_{i_2}(X) \ \dots \ A_{i_K}(X)] \in \mathbb{R}^{M \times P}, \quad P = \sum_{k=1}^K p_{i_k},$$

where each $A_{i_k}(X) \in \mathbb{R}^{M \times p_{i_k}}$ denotes the corresponding layer output evaluated at the M spatial points in X . This allows the basis to combine features from multiple depths. When needed, we further append a column of ones to include a constant basis function, so that spatially uniform components are represented explicitly.

Analytic derivatives for PDE operators. PDE assembly requires spatial derivatives of the neural basis. Here, for each layer $\ell = 0, \dots, L$, we denote the Jacobian and Hessian by

$$J_\ell(X) \in \mathbb{R}^{M \times p_\ell \times d}, \quad H_\ell(X) \in \mathbb{R}^{M \times p_\ell \times d \times d},$$

where $J_\ell(X)_{m, :, i}$ and $H_\ell(X)_{m, :, i, j}$ store the first- and second-order derivatives of the layer- ℓ outputs at x_m . These quantities are propagated analytically through the residual network. For the nonlinear branch $z_\ell(X) = \sigma(a_\ell(X))$, we use

$$\frac{\partial z_\ell}{\partial t_\ell} = \sigma'(a_\ell) \odot \alpha_\ell^T, \quad \frac{\partial^2 z_\ell}{\partial t_\ell^2} = \sigma''(a_\ell) \odot (\alpha_\ell^2)^T,$$

with all operations acting elementwise. In the first layer, the skip branch contributes a constant Jacobian and zero Hessian; for deeper layers, $J_{\ell-1}(X)$ and $H_{\ell-1}(X)$ are propagated through the linear and nonlinear branches by the chain rule. This yields analytic gradients, divergences, and Laplacians at the points in X , without numerical or automatic differentiation.

Neural basis initialization. The fixed neural basis is constructed by explicitly initializing the parameters $\{W_\ell, b_\ell, P_\ell\}_{\ell=1}^L$. For layers $\ell \geq 2$, the entries of W_ℓ are sampled independently from $\mathcal{N}(0, 1)$, the entries of b_ℓ independently from the uniform distribution on $[-r, r]$, where $r > 0$ is a prescribed radius parameter, and P_ℓ is taken as the identity when $p_\ell = p_{\ell-1}$ and otherwise sampled from a zero-mean Gaussian distribution with variance scaled by $1/\sqrt{p_{\ell-1}}$. The first layer is treated separately to reduce geometric redundancy, since each neuron defines an affine function whose zero level set is a hyperplane and naive random initialization can produce nearly coincident or strongly correlated features. To avoid this, candidate first-layer neurons are filtered by simple geometric diversity criteria; in two dimensions, we exclude lines with negligible intersection length and lines that are nearly parallel to or spatially clustered with previously accepted ones.

First-layer scaling. To make the first-layer basis independent of the size and location of the physical domain $\Omega = [x_1, \bar{x}_1] \times \dots \times [x_d, \bar{x}_d] \subset \mathbb{R}^d$, we define it with respect to the normalized

reference domain $[-1, 1]^d$. Let $s_i = (\bar{x}_i - \underline{x}_i)/2$ and $c_i = (\bar{x}_i + \underline{x}_i)/2$, so that $\hat{x}_i = (x_i - c_i)/s_i \in [-1, 1]$. Rather than rescaling coordinates explicitly, we absorb this affine map into the first-layer parameters: if $W_{1,0}$, $P_{1,0}$, and $b_{1,0}$ are defined on the reference domain, then $W_1 = W_{1,0} \text{diag}(s)^{-1}$, $P_1 = P_{1,0} \text{diag}(s)^{-1}$, and $b_1 = b_{1,0} - W_{1,0}(c \oslash s)$, with \oslash denoting elementwise division. Since the skip branch is linear in the input coordinates, this rescaling also induces a constant shift, so we evaluate $s_1(X) = \beta_1(XP_1^T) + \mathbf{1}\gamma_1^T$, with $\gamma_1 = -\beta_1 P_{1,0}(c \oslash s)$. For the axis-aligned rectangular domains considered here, this mapping is exact, ensuring that the first-layer basis is defined consistently on $[-1, 1]^d$, while no further domain-dependent scaling is needed in deeper layers.

Appendix C: Geometric interpretation and conditioning effect of dual-layer neural basis

Geometric interpretation. Single-layer neural bases admit a geometric interpretation through the induced hyperplanes [15, 25, 60]. A random ensemble of such hyperplanes produces a soft partition of the domain, with each basis transitioning rapidly but smoothly across its associated hyperplane. However, random initialization can generate near-duplicate hyperplanes, leading to highly correlated features and ill-conditioned projection systems. To mitigate this while retaining the underlying hyperplane-induced geometry, we introduce a second linear–nonlinear map that recombines the first-layer features. Specifically, for each second-layer node $k = 1, \dots, N_2$, we define $z_k(\mathbf{x}) = \sum_{j=1}^{N_1} W_{kj}^{(2)} \phi_j^{(1)}(\mathbf{x}) + b_k^{(2)}$ and $\phi_k^{(2)}(\mathbf{x}) = \sigma(z_k(\mathbf{x}))$. Thus, $z_k(\mathbf{x})$ is a fixed superposition of first-layer hyperplane responses, whose level sets encode a composite soft partition of the domain, while $\phi_k^{(2)}(\mathbf{x})$ is a bounded nonlinear transformation of this aggregated signal. In this way, the second layer preserves the geometric organization inherited from the first layer while reducing collinearity and improving conditioning. The final PDE solution is then represented as a linear combination of $\{\phi_k^{(2)}\}$. In our implementation, the rows of $\mathbf{W}^{(2)} \in \mathbb{R}^{N_2 \times N_1}$ are sampled from $\mathcal{N}(0, 1)$ and $\mathbf{b}^{(2)} \in \mathbb{R}^{N_2}$ from $[-r, r]$, after which all parameters are kept fixed. Fig. C.1 illustrates this construction through first-layer features, second-layer pre-activation fields, and the corresponding dual-layer architecture. Red connections highlight how first-layer features are superposed to form z_k , and applying the activation produces the corresponding post-activation basis function $\phi_k^{(2)}(\mathbf{x}) = \sigma(z_k(\mathbf{x}))$ that enters the final expansion. This dual-layer architecture with the fixed linear–nonlinear recombination yields dramatically improved conditioning in the resulting projection systems compared with using $\{\phi_j^{(1)}\}$ directly, while retaining a clear geometric link to the first-layer hyperplane partition.

Conditioning effect. Depth in the neural basis has a pronounced effect on the conditioning of the neural projection system as the basis size N_b increases. Using the same setup of Fig. 3a, we compare single-layer, dual-layer, and triple-layer cases. Fig. C.2 shows that the single-layer case becomes rapidly ill-conditioned, with the condition number reaching 3.34×10^{13} at $N_b = 1000$, whereas adding one additional layer reduces it to 5.76×10^8 at the same basis size, and a triple-layer basis further reduces it to 9.25×10^6 at $N_b = 2000$. For the dual-layer and triple-layer cases, all hidden layers are chosen to have the same width so that the comparison isolates the effect of depth rather than incidental width imbalance or bottleneck effects. Under this controlled setting, the improved conditioning is primarily attributable to the reduced basis correlation induced by multi-layer recombination. A complementary geometric view also suggests that, for the low-dimensional physical domains relevant to most engineering PDEs, raw partition count is unlikely to be the main bottleneck at basis sizes on $O(10^3)$. With N_1 hyperplanes, the maximal number of induced partitions in \mathbb{R}^d is $P_d(N_1) = \sum_{k=0}^d \binom{N_1}{k}$. For example, $N_1 = 1000$ already yields 1001, 500,501, and 166,667,501 partitions in $d = 1, 2, 3$, respectively.

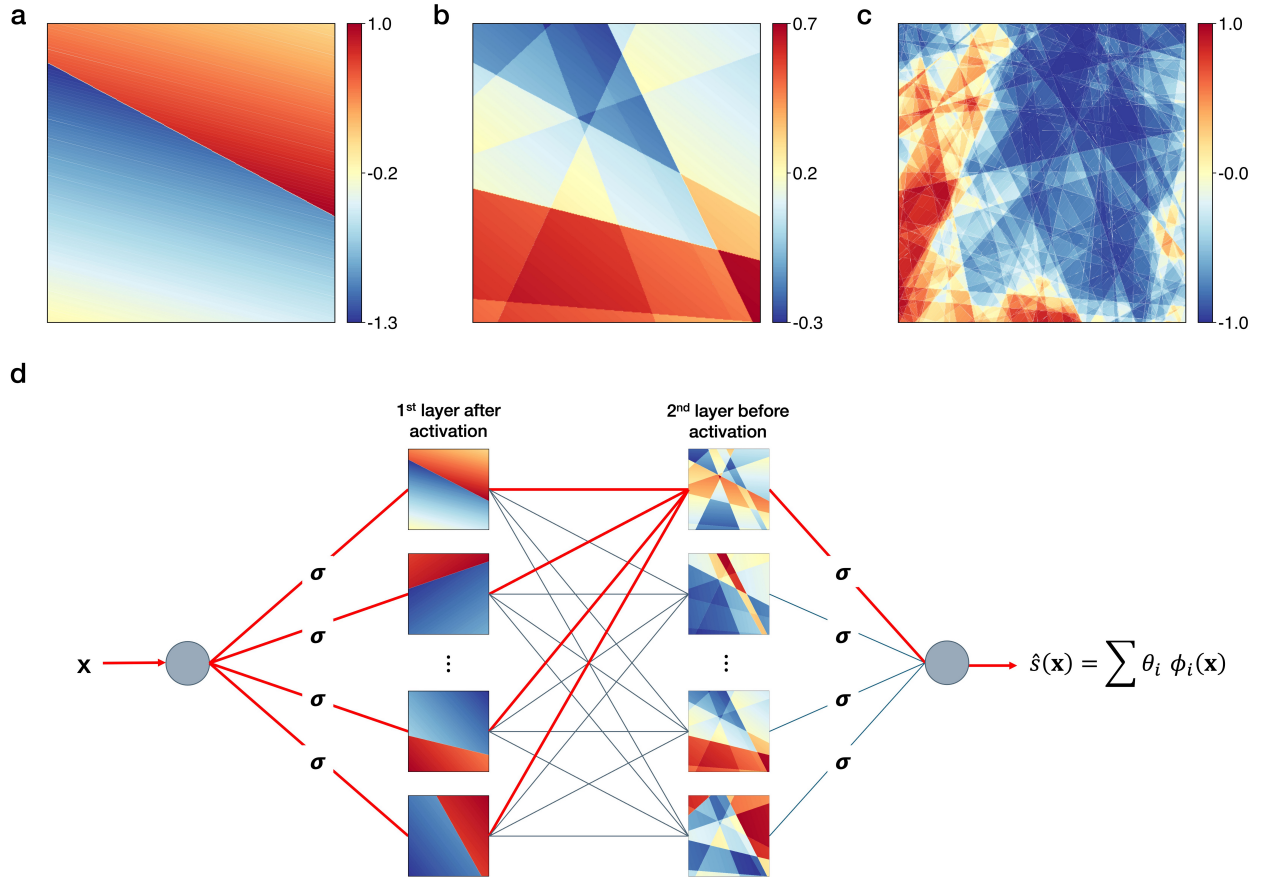


Fig. C.1 | Geometric illustration of dual-layer neural basis. **a**, A first-layer hyperplane after activation. **b**, A second-layer pre-activation field formed by superposing $N_1 = 10$ first-layer features. **c**, A second-layer pre-activation field formed with $N_1 = 200$ first-layer features. **d**, Schematic of dual-layer basis generator: input produces first-layer hyperplanes, superpositions form pre-activations fields, and post-activation outputs the final basis functions.

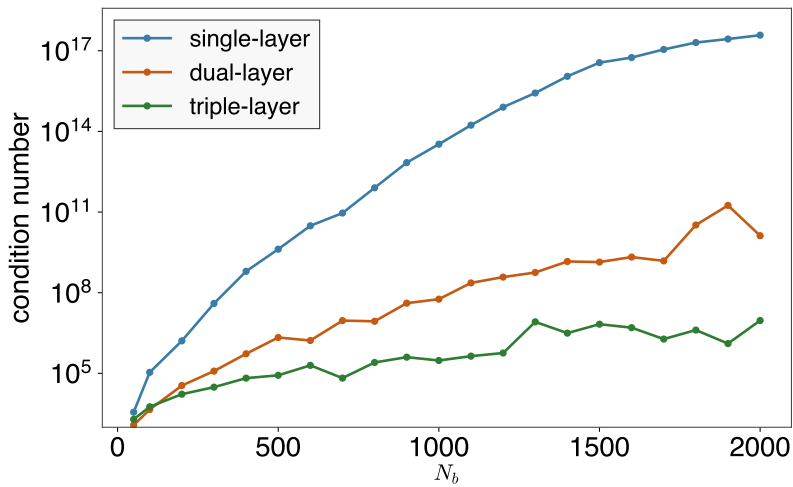


Fig. C.2 | Effect of depth in neural basis generation on numerical conditioning. Condition number of the assembled neural projection system versus neural basis size N_b for single-layer, dual-layer, and triple-layer basis generators (logarithmic y -axis).

Appendix D: Expressivity and stability of neural basis space

Here, we assess how a given neural basis space represents the target pressure, mass-flux, and concentration fields. We use the setup shown in Fig. 3a and take the corresponding solution snapshots at day 10 as the reference fields.

Least-squares projection and best-approximation error. We assess neural basis expressivity by the smallest discrete relative L_2 error attainable in approximating the reference fields. For a target scalar field $s(\mathbf{x})$ (pressure, a mass-flux component, or concentration) sampled at M collocation points, we build the basis evaluation matrix $\Phi \in \mathbb{R}^{M \times N_b}$ with $\Phi_{ji} = \phi_i(\mathbf{x}_j)$ and perform a projection problem: $\boldsymbol{\theta}^* = \arg \min_{\boldsymbol{\theta} \in \mathbb{R}^{N_b}} \|\Phi \boldsymbol{\theta} - \mathbf{s}_{\text{ref}}\|_2^2$ and $\widehat{s}(\mathbf{x}) = \sum_{i=1}^{N_b} \theta_i^* \phi_i(\mathbf{x})$. Here $\mathbf{s}_{\text{ref}} \in \mathbb{R}^M$ collects the reference values $s_{\text{ref}}(\mathbf{x}_j)$. The resulting $\|\widehat{s} - s_{\text{ref}}\|_2 / \|s_{\text{ref}}\|_2$ is thus the minimum discrete relative L_2 error achievable under the chosen sampling and norm. For the mass-flux $\mathbf{q} = (q_x, q_y)$, we evaluate expressivity componentwise. When no Helmholtz decomposition is used, we apply the projection separately to q_x and q_y . When Helmholtz decomposition is used, we first write the reference flux as $\mathbf{q}_{\text{ref}} = \mathbf{q}_{\text{ref}}^{(\text{div})} + \mathbf{q}_{\text{ref}}^{(\text{curl})}$, then project the four scalar components $q_{x,\text{ref}}^{(\text{div})}$, $q_{y,\text{ref}}^{(\text{div})}$, $q_{x,\text{ref}}^{(\text{curl})}$, and $q_{y,\text{ref}}^{(\text{curl})}$ in their corresponding neural basis spaces, and finally reconstruct $\widehat{\mathbf{q}}$ by summation. We report relative L_2 projection errors for q_x , q_y , and $|\mathbf{q}|$, together with the associated condition numbers of the respective projections.

Pressure projection: dual-layer versus single-layer bases. Because pressure is smooth and dominated by low-frequency content, both single- and dual-layer bases approximate the reference field very well. The reference pressure p_{ref} is shown in Fig. D.1a, and the corresponding absolute projection errors $|\widehat{p} - p_{\text{ref}}|$ for the dual-layer and single-layer bases are shown in Fig. D.1b–c. As summarized in Fig. D.1d, replacing the dual-layer basis with the single-layer basis increases the best-approximation error only slightly, from 0.001% to 0.0011%, but increases the condition number much more severely, from 2.6×10^8 to 1.7×10^{15} . The main difference is therefore not approximation quality but numerical conditioning, and in the PDE-constrained least-squares projection such ill-conditioning can amplify numerical noise and destabilize the solution coefficient updates.

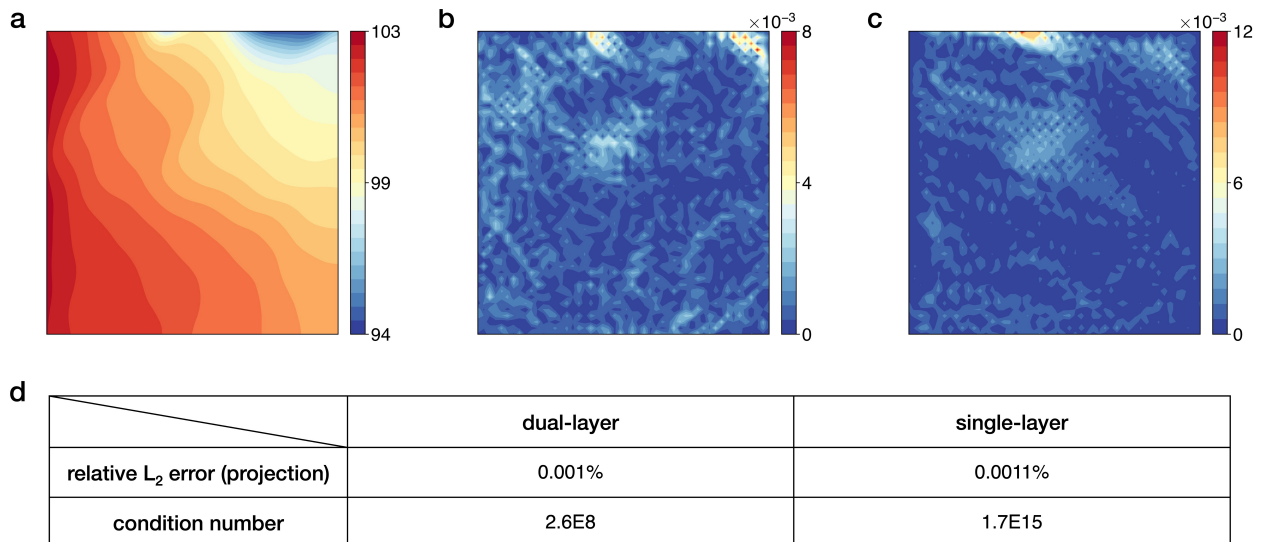


Fig. D.1 | Neural basis expressivity and stability for pressure. a, FVM reference pressure p (bar). b–c, Absolute projection error using dual-layer and single-layer scalar neural basis, respectively. d, Relative L_2 projection error and condition number of the projection system. **Note:** Pressure is reported in bar.

Mass-flux projection: dual-layer versus single-layer bases, with and without Helmholtz split. The mass-flux projection highlights two practically important effects: the Helmholtz split improves best-approximation, while the single-layer basis can substantially worsen conditioning. The reference magnitude $|\mathbf{q}_{\text{ref}}|$ and the componentwise absolute projection errors for q_x and q_y are shown in Fig. D.2a–e, and the relative L_2 errors together with the condition numbers are summarized in Fig. D.2f. Within each basis generator, introducing the Helmholtz split reduces the projection error. For the dual-layer basis, the relative errors decrease from 1.00% to 0.86% for q_x , from 1.66% to 1.21% for q_y , and from 1.10% to 0.80% for $|\mathbf{q}|$; for the single-layer basis, they decrease from 1.29% to 1.01%, from 1.92% to 1.48%, and from 1.35% to 1.06%, respectively. With the Helmholtz split, replacing the dual-layer basis by the single-layer basis still increases the best-approximation error, from 0.86% to 1.01% for q_x , from 1.21% to 1.48% for q_y , and from 0.80% to 1.06% for $|\mathbf{q}|$, while conditioning deteriorates much more severely: for q_x , the div-free block increases from 2.6×10^8 to 1.2×10^{13} and the curl-free block from 6.3×10^6 to 8.0×10^{12} , with similar behavior for q_y . Without the Helmholtz split, replacing the dual-layer basis by the single-layer basis increases the relative errors from 1.00% to 1.29% for q_x , from 1.66% to 1.92% for q_y , and from 1.10% to 1.35% for $|\mathbf{q}|$, while the condition number rises from 2.6×10^8 to 1.7×10^{15} . Compared with pressure, the mass-flux errors are a few orders of magnitude larger, which is expected because \mathbf{q} is less smooth: it depends on pressure gradients and multiscale permeability, both of which amplify high-frequency content. This is also reflected in Fig. D.2g, where the projected and reference spectra agree well over the dominant low-to-intermediate wavenumbers, while the remaining discrepancy is concentrated in the high-wavenumber tail.

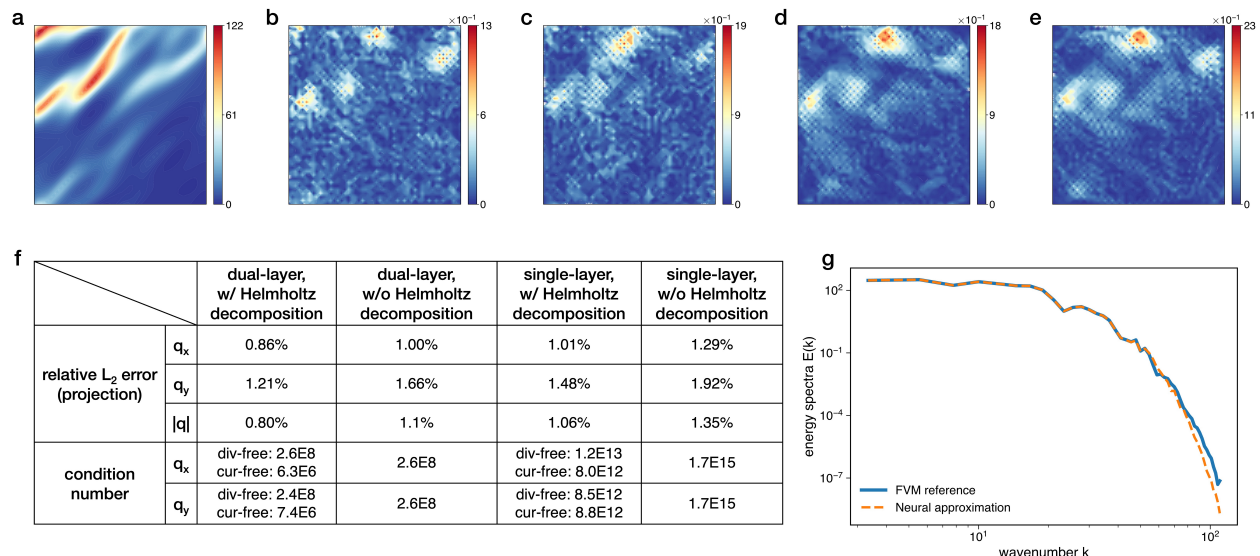


Fig. D.2 | Neural basis expressivity and stability for mass-flux. **a**, FVM reference ($\text{kg m}^{-2} \text{s}^{-1}$). **b–e**, Absolute projection error using dual-layer neural vector basis w/ Helmholtz decomposition, dual-layer neural vector basis w/o Helmholtz decomposition, single-layer neural vector basis w/ Helmholtz decomposition, and single-layer neural vector basis w/o Helmholtz decomposition, respectively. **f**, Relative L_2 projection errors for q_x , q_y , and $|\mathbf{q}|$ and condition numbers of the corresponding projection systems. **g**, Energy spectra $E(k)$ of the reference and the best projected mass-flux fields. **Note:** Mass-flux is reported in $\text{kg day}^{-1} \text{m}^{-2}$.

Concentration projection: dual-layer versus single-layer bases and the effect of stabilization. Concentration projection behaves differently from pressure and mass flux because sharp advective fronts limit the best-approximation power of smooth neural bases. However, stabilization can make the target more compatible with the smooth neural bases and reduce projection error

markedly. The reference concentration, the corresponding projection errors of the dual-layer and single-layer bases, and the error-conditioning summary are shown in Fig. D.3a–d. Replacing the dual-layer basis by the single-layer basis increases the best-approximation error only slightly, from 0.92% to 0.99%, but increases the condition number severely, from 2.6×10^8 to 1.7×10^{15} . The larger approximation difficulty comes instead from the limited regularity of advective concentration fields: direct projection of a sharp produces substantially larger error, as shown in Fig. D.3e,g,i,k, because such interfaces are difficult for a smooth neural expansion to represent. In the NBM transport discretization, first-order upwinding introduces numerical stabilization by creating a narrow grid-scale transition zone, thereby replacing the discontinuous step by a profile with finite transition thickness. This makes the target much more compatible with the neural basis, and accordingly a five-cell smeared front yields a much smaller projection error, as shown in Fig. D.3f,h,j,k. The remaining discrepancy is localized near the stabilized interface. Fig. D.3k also highlights that the sharp-front and five-cell smeared profiles appear visually similar, yet their relative L_2 difference is 9.19%, while the best-approximation error for projecting the discontinuous front is 7.73%. Overall, these results show that transport benefits substantially from stabilization and that the neural basis represents the stabilized transport profile with low error.

Appendix E: Construction and effect of physics-conforming neural vector bases

Construction. Given scalar neural basis functions $\{\phi_i(\mathbf{x})\}$, we construct curl-free and divergence-free neural vector bases by applying differential operators directly to the scalar basis. In 2D, we define

$$\phi_i^{(\text{curl})}(\mathbf{x}) = \nabla \phi_i(\mathbf{x}) = \begin{bmatrix} \partial_x \phi_i(\mathbf{x}) \\ \partial_y \phi_i(\mathbf{x}) \end{bmatrix}, \quad \phi_i^{(\text{div})}(\mathbf{x}) = \nabla^\perp \phi_i(\mathbf{x}) = \begin{bmatrix} \partial_y \phi_i(\mathbf{x}) \\ -\partial_x \phi_i(\mathbf{x}) \end{bmatrix},$$

so that $\nabla \times \phi_i^{(\text{curl})} \equiv 0$ and $\nabla \cdot \phi_i^{(\text{div})} \equiv 0$. The resulting mass-flux representation takes the form

$$q_{x,NN}(\mathbf{x}) = \sum_i \left[\theta_i^{(\text{div})} \partial_y \phi_i(\mathbf{x}) + \theta_i^{(\text{curl})} \partial_x \phi_i(\mathbf{x}) \right], \quad q_{y,NN}(\mathbf{x}) = \sum_i \left[-\theta_i^{(\text{div})} \partial_x \phi_i(\mathbf{x}) + \theta_i^{(\text{curl})} \partial_y \phi_i(\mathbf{x}) \right].$$

In 3D, the curl-free counterpart is constructed in the same way as the 2D case. However, for the divergence-free counterpart, we use vector potentials for the construction. For each ϕ_i , we define $\mathbf{F}_i^{(x)}(\mathbf{x}) = \mathbf{e}_x \phi_i(\mathbf{x})$, $\mathbf{F}_i^{(y)}(\mathbf{x}) = \mathbf{e}_y \phi_i(\mathbf{x})$, and $\mathbf{F}_i^{(z)}(\mathbf{x}) = \mathbf{e}_z \phi_i(\mathbf{x})$, with $\mathbf{e}_x = (1, 0, 0)^\top$, $\mathbf{e}_y = (0, 1, 0)^\top$, and $\mathbf{e}_z = (0, 0, 1)^\top$. We then take curls to obtain

$$\phi_i^{(\text{div},x)} = \nabla \times \mathbf{F}_i^{(x)} = \begin{bmatrix} 0 \\ \partial_z \phi_i \\ -\partial_y \phi_i \end{bmatrix}, \quad \phi_i^{(\text{div},y)} = \nabla \times \mathbf{F}_i^{(y)} = \begin{bmatrix} -\partial_z \phi_i \\ 0 \\ \partial_x \phi_i \end{bmatrix}, \quad \phi_i^{(\text{div},z)} = \nabla \times \mathbf{F}_i^{(z)} = \begin{bmatrix} \partial_y \phi_i \\ -\partial_x \phi_i \\ 0 \end{bmatrix},$$

each of which is divergence-free by construction. The divergence-free and curl-free parts of the flux are then represented as

$$\mathbf{q}_{NN}^{(\text{div})}(\mathbf{x}) = \sum_i \left(\theta_i^{(\text{div},x)} \phi_i^{(\text{div},x)}(\mathbf{x}) + \theta_i^{(\text{div},y)} \phi_i^{(\text{div},y)}(\mathbf{x}) + \theta_i^{(\text{div},z)} \phi_i^{(\text{div},z)}(\mathbf{x}) \right),$$

$$\mathbf{q}_{NN}^{(\text{curl})}(\mathbf{x}) = \sum_i \theta_i^{(\text{curl})} \phi_i^{(\text{curl})}(\mathbf{x}).$$

Effect. We assess the effect of the physics-conforming construction using the setups provided in Fig. 2a and Fig. 3a. As summarized in Table E.1, we report (i) the conservation residuals from the least-squares solve, (ii) relative L_2 errors or differences for pressure (p), velocity (u_x and u_y), and concentration (c), and (iii) spectral discrepancy metrics, namely the relative spectral error and the Kolmogorov–Smirnov (K–S) distance. The conservation residual is evaluated from the fitted least-squares residual vector $\mathcal{E} = \mathbf{A}\boldsymbol{\theta}^* - \mathbf{b}$ by extracting the entries associated with the mass-balance equations and computing the normalized quantity $\mathcal{E}_{\text{rel}}^{\text{cons}} = \|\mathcal{E}_{\text{cons}}\|_2^2 / \|\mathbf{b}\|_2^2$. For the

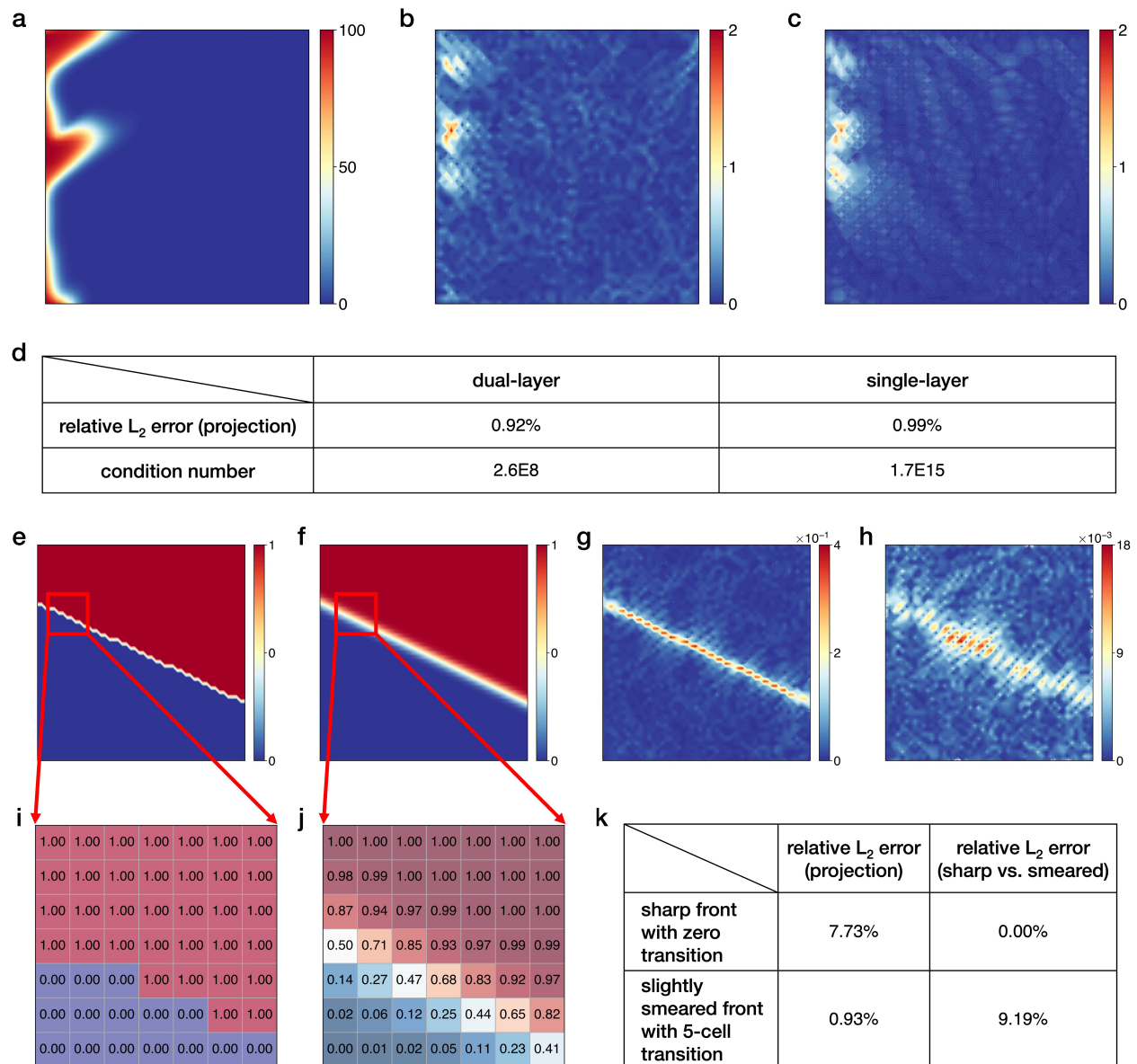


Fig. D.3 | Neural-basis expressivity and stability for concentration. **a**, FVM reference. **b-c**, Absolute projection error using dual-layer and single neural scalar basis, respectively. **d**, Relative L_2 projection error and condition number of the projection system. **e**, Sharp-front field with zero transition thickness (discontinuous step). **f**, Slightly smeared front with a 5-cell transition (stabilized profile). **g-h**, Absolute projection error for sharp-front and smeared-front cases, respectively. **i-j**, Cell values near sharp-front and smeared-front, respectively. **k**, Relative L_2 projection errors for the sharp-front and smeared-front fields, and the relative L_2 difference between the two fields (sharp vs. smeared). **Note:** Concentration is reported in ppm.

heterogeneous case, we report relative L_2 differences rather than errors, since no mesh-converged ground truth is available for the discrete-valued heterogeneous field and the finite-volume solution on the same spatial resolution is used as the reference baseline. Overall, Table E.1 shows that enforcing the physics-conforming vector structure substantially reduces conservation residuals and improves solution quality, with especially strong gains in the heterogeneous setting, including clear reductions in concentration error and spectral mismatch. In incompressible settings, the benefit is even more immediate, since the divergence-free constraint is represented exactly by construction and can remove the need for a separate conservation equation in the least-squares system when source and sink terms are imposed as internal boundary conditions.

Table E.1 | Effect of physics-conforming neural vector bases.

		conservative residual	p (%)	u_x (%)	u_y (%)	c (%)	spectral (%)	K-S distance
Homogeneous (Fig. 2a)	w/ physics-conforming	9.92E-12	0.001	0.16	0.30	5.17	0.02	2.45E-5
	w/o physics-conforming	1.34E-9	0.0016	0.12	0.35	5.30	0.03	2.48E-5
Heterogeneous (Fig. 3a)	w/ physics-conforming	6.17E-11	0.045	1.96	3.03	4.09	0.91	0.002
	w/o physics-conforming	7.93E-8	0.11	3.89	5.18	8.70	4.69	0.003

Appendix F: Carbon storage example setups

We consider a supercritical CO_2 storage benchmark in the square porous domain $\Omega = [0, 762] \text{ m} \times [0, 762] \text{ m}$ under two permeability settings: (i) a homogeneous case with constant permeability $\kappa = 0.3 \text{ D}$ (Fig. 2a), and (ii) a heterogeneous case in which $\kappa(\mathbf{x})$ is given by a geologically realistic Gaussian random field (Fig. 3a), with permeability contrast 502. A passive tracer is injected from the left boundary, and all other settings are identical between the two cases.

Boundary conditions. On the left boundary ($x = 0$), we prescribe pressure $p = 103.4 \text{ bar}$ and a passive tracer pulse with concentration $c_{\text{in}} = 100 \text{ ppm}$ during the first 10 days. On the top boundary ($y = 762 \text{ m}$), we impose an outward mass-flux $q_y = 586 \text{ kg day}^{-1} \text{ m}^{-2}$. The right boundary ($x = 762 \text{ m}$) is no-flow ($q_x = 0$), and the bottom boundary ($y = 0$) is no-flow ($q_y = 0$).

Porous media and fluid properties. Besides the permeability field, other porous media and fluid properties are uniform: porosity $\varepsilon = 0.25$, viscosity $\mu = 0.04 \text{ cP}$, compressibility $c_f = 2.90 \times 10^{-3} \text{ bar}^{-1}$, and reference density $\rho_0 = 384 \text{ kg m}^{-3}$ at $50 \text{ }^\circ\text{C}$ and $p_0 = 103.4 \text{ bar}$.

Reference and discretizations. For the homogeneous case, we use an finite-volume solution on a 1000×1000 structured uniform mesh as a ground-truth proxy. For the heterogeneous case, an analogous fine-grid ground truth is not available by refinement, since the permeability is specified through a discrete heterogeneous realization rather than a known continuous field. In both cases, the baseline finite-volume solution is computed on a 50×50 structured uniform mesh. For NBM, we use collocation on a matching 50×50 uniform interior grid (2500 interior points), together with 50 uniformly distributed collocation points on each boundary, for a total of 2700 collocation points. The vanilla PINN baselines use the same spatial resolution. For comparisons involving the energy-consistent weight (9), the baseline choice is uniform weighting with all weights set to 1.

Appendix G: Manufactured-solution benchmark

To quantify accuracy in a multiscale setting where grid refinement does not provide ground-truth proxy, we introduce a manufactured-solution benchmark based on the simplified incompressible system $\mathbf{u} = -(\kappa(x, y)/\mu)\nabla p$ and $\nabla \cdot \mathbf{u} = 0$ on a regular domain Ω with constant viscosity μ . The permeability is chosen as a separable multiscale field $\kappa(x, y) = a(x)b(y)$, where the smooth oscillatory 1D factors are given by $a(x) = \exp\left(s_x \frac{\varphi_x(x)}{\max|\varphi_x|}\right)$ and $b(y) = \exp\left(s_y \frac{\varphi_y(y)}{\max|\varphi_y|}\right)$, with $\varphi_x(x) = \beta_{x1} \sin(2\pi x) + \beta_{x2} \cos(4\pi x)$, $\varphi_y(y) = \beta_{y1} \cos(2\pi y) + \beta_{y2} \sin(2\pi y)$, and $s_x = \frac{1}{2} \log(\mathcal{C}_x)$, $s_y = \frac{1}{2} \log(\mathcal{C}_y)$ controlling the 1D contrasts \mathcal{C}_x and \mathcal{C}_y . All permeability values are evaluated at cell centers of a uniform grid. An exact pressure field is then manufactured from the antiderivatives $I_x(x) = \int_{x_{\min}}^x \frac{1}{a(s)} ds$ and $I_y(y) = \int_{y_{\min}}^y \frac{1}{b(s)} ds$ by setting $p(x, y) = p_0 + B(C_x I_x(x) + C_y I_y(y))$, where p_0 is a reference pressure, B sets the amplitude, and C_x, C_y control the relative strengths of the two coordinate contributions. This gives $\partial_x p = B \frac{C_x}{a(x)}$ and $\partial_y p = B \frac{C_y}{b(y)}$, and hence the analytic velocity field $u_x(x, y) = -\frac{BC_x}{\mu} b(y)$ and $u_y(x, y) = -\frac{BC_y}{\mu} a(x)$, so that u_x depends only on y , u_y depends only on x , and the divergence-free constraint holds identically. Boundary conditions for p are taken directly from the manufactured pressure, and the benchmark therefore admits an exact solution pair (p, \mathbf{u}) for any prescribed contrasts and coefficients.

In implementation, the permeability is assembled on cell centers as $\kappa_{ij} = k_0 a(x_i)b(y_j)$ with uniform scaling factor k_0 . The integrals I_x and I_y are evaluated on the corresponding 1D grids to construct p_{ij} at cell centers, using either cumulative trapezoidal integration on the uniform grid or higher-accuracy piecewise Gauss–Legendre 8-point quadrature on each cell interval. The exact velocity is evaluated from the closed-form expressions above, avoiding numerical differencing.

For the experiments of Fig. 3k–s, we set $\Omega = [-1, 1] \times [-1, 1]$, $p_0 = 34$ bar, $\mu = 1.0$ cp, $B = -20$, $(C_x, C_y) = (1.0, -0.6)$, and $k_0 = 0.1$. The permeability contrasts are sets as $\mathcal{C}_x = \max(a)/\min(a) = 200$ and $\mathcal{C}_y = \max(b)/\min(b) = 20$, yielding an overall contrast of about 1078; varying $(\mathcal{C}_x, \mathcal{C}_y)$ generates fields with different contrast levels. This benchmark provides exact pressure and velocity only. The concentration reference is obtained by solving the transport equation with an finite-volume discretization using first-order upwinding driven by the manufactured velocity field, since an exact closed-form concentration solution is generally unavailable for heterogeneous advection under general initial and boundary conditions.

Appendix H: NBM–OL implementation and experiment configuration

The NBM–OL implementation follows the structured workflow summarized in Fig. 4. We consider three operator-learning settings: **Case-I**, a permeability-varying steady Darcy flow operator; **Case-II**, a boundary-flux-varying Darcy flow operator; and **Case-III**, a boundary-flux/concentration-varying Darcy–transport operator. Across all cases, NBM–OL learns a map from the problem parameters (and time, when applicable) to solution coefficients in the neural basis space, enabling rapid inference of pressure, flux/velocity, and concentration fields.

The common workflow is as follows: (i) define a parameterization of the operator family; (ii) generate coefficient snapshots by solving sampled training instances using NBM; (iii) apply POD blockwise to compress the coefficient snapshots into latent coordinates; (iv) train an MLP operator in the latent space using the residual metric \mathcal{E}_{rel} as a self-supervised objective; and (v) at inference, predict the latent coordinates, reconstruct the full coefficients, and recover the solution fields by

neural basis expansion. When POD compression is not used, steps (ii) and (iii) are omitted.

All experiments use the square domain $\Omega = [0, 762] \text{ m} \times [0, 762] \text{ m}$. Interior residuals are evaluated on a structured 100×100 collocation set (10,000 points), and boundary residuals on 400 uniformly distributed boundary points with corners excluded. Pressure, mass-flux (or velocity in the incompressible case), and concentration are represented by separate neural bases, all with size $N_b = 800$. When POD is used, it is applied separately to each coefficient block. OOD tests are constructed by extending one or more parameter axes and/or the time horizon beyond the training ranges.

Case-I: permeability-varying steady Darcy flow operator. We impose mixed boundary conditions: $p = 69$ bar on $x = 0$, $u_x = 0.3 \text{ m day}^{-1}$ on $x = 762 \text{ m}$, and $u_y = 1.5 \text{ m day}^{-1}$ on $y = 0$ and $y = 762 \text{ m}$, using the outward-normal sign convention. The base permeability template $\kappa_{\text{ref}}(\mathbf{x})$ is defined on a 100×100 grid, and heterogeneity is parameterized by a piecewise-constant 5×5 blockwise field (block25) generated from a Gaussian random field. Each block25 realization is upsampled by block repetition and applied multiplicatively to $\kappa_{\text{ref}}(\mathbf{x})$. We generate $N_s = 1000$ realizations and compute steady NBM coefficient snapshots $(\boldsymbol{\theta}_{\text{div}}, \boldsymbol{\theta}_p)$; only the divergence-free velocity block is needed because this setup is incompressible. POD retains $r_p = 16$ and $r_q = 16$ modes, yielding $\mathbf{z} = [\mathbf{z}_p; \mathbf{z}_q] \in \mathbb{R}^{32}$. The latent map is learned by a two-branch MLP, one branch for pressure and one for velocity, each with two hidden layers of width 64 and tanh activation. Training uses Adam with learning rate 10^{-3} , batch size 16, and 500 epochs. OOD tests are generated by perturbing the Gaussian random field controls, including variance/contrast scaling, correlation-length changes, and rotation-angle shifts.

Case-II: boundary-flux-varying Darcy flow operator. The operator family is parameterized by a scalar top-boundary mass-flux control g_{top} , uniformly sampled from $[488, 976] \text{ kg day}^{-1} \text{ m}^{-2}$. We prescribe $p = 103$ bar on $x = 0$ and impose no-flux conditions on the right and bottom boundaries. The permeability field is fixed and multiscale on a 100×100 grid. We generate $N_s = 200$ scenarios, each simulated for $N_{\text{Darcy}} = 20$ Darcy time steps with $\Delta T = 10.0$ days, yielding $N_{\text{snap}} = 4000$ snapshots for each coefficient block $(\boldsymbol{\theta}_{\text{div}}, \boldsymbol{\theta}_{\text{curl}}, \boldsymbol{\theta}_p)$. POD retains $r_{\text{div}} = 8$, $r_{\text{curl}} = 8$, and $r_p = 8$ modes, giving $\mathbf{z} = [\mathbf{z}_{\text{div}}; \mathbf{z}_{\text{curl}}; \mathbf{z}_p] \in \mathbb{R}^{24}$. The latent operator $\mathcal{F}(g_{\text{top}}, t)$ is represented by three MLP branches, each with two hidden layers of width 32 and tanh activation. Training uses Adam with learning rate 10^{-3} , batch size 16, and 500 epochs. OOD evaluation extends the g_{top} range by 50% and the prediction horizon by 100% beyond the training ranges.

Case-III: boundary-flux/concentration-varying Darcy–transport operator. The coupled operator family is parameterized by $(g_{\text{top}}, c_{\text{left}})$, where g_{top} is the top-boundary Darcy mass-flux control and c_{left} is the injected tracer concentration on the left boundary, sampled from $\mathcal{U}(50.0, 100.0)$ ppm. The Darcy boundary setup and fixed permeability field are the same as in Case-II unless stated otherwise. We generate $N_s = 80$ independent scenarios. For each g_{top} , the pretrained Case-II model is used to infer the Darcy velocity sequence, and each Darcy time step is split into $N_{\text{tr}} = 8$ transport substeps. We use $N_{\text{Darcy}} = 10$ Darcy coarse steps, so the total number of transport substeps is $N_{\text{sub}} = N_{\text{Darcy}} N_{\text{tr}}$. POD is applied to the transport coefficient snapshots $\{\boldsymbol{\theta}_c\}$ and retains $r_c = 20$ modes, yielding $\mathbf{z}_c \in \mathbb{R}^{20}$. The latent map $\mathbf{z}_c(t) = \mathcal{F}(g_{\text{top}}, c_{\text{left}}, t_{\text{norm}})$ is learned by a single MLP with two hidden layers of width 64, tanh activation, and weight normalization. Training uses Adam with learning rate 5×10^{-3} , batch size 32, and 1000 epochs. OOD evaluation extends both $(g_{\text{top}}, c_{\text{left}})$ by 50% and the prediction horizon by 100% beyond the training ranges.

Appendix I: Physics-informed neural network (PINN) baseline

We use a two-network, two-stage vanilla PINN baseline for the coupled Darcy–transport problem. In Stage A, pressure is approximated by a neural network $p(\cdot; \omega_p)$ and trained by minimizing a weighted sum of mean-squared residuals at collocation points, consisting of the strong-form slightly compressible Darcy residual in the interior together with boundary penalties enforcing the left Dirichlet pressure condition and mass-flux conditions on the other boundaries, where the normal mass flux is obtained from ∇p via automatic differentiation. In Stage B, concentration is approximated by a second network $c(\cdot; \omega_c)$; after freezing ω_p , we train ω_c using a conservative transport residual at space–time collocation points, together with penalties enforcing the initial condition $c(\cdot, 0) = 0$ and the time-dependent inlet Dirichlet condition on the left boundary. To reduce cost while preserving PDE-level coupling, once Stage A converges we precompute the mass-flux components and their divergence induced by $p(\cdot; \omega_p)$ on the full space–time collocation set and reuse them throughout Stage B, so that only $c(\cdot; \omega_c)$ is differentiated during transport training.

Both networks are fully connected MLPs with tanh activations, width 64, depth 4, and scalar output, taking (x, y, t) as input. Collocation uses a fixed 50×50 spatial grid of cell centers and $N_t = 10$ time levels, giving $50 \times 50 \times 10$ interior space–time points, while boundary collocation points are the boundary cell centers replicated across the same time levels. For Stage A, we use Adam with learning rate 10^{-3} for 20,000 iterations with mini-batches of size 4096 for interior points and 1024 for each boundary set, followed by full-batch L-BFGS for 2,000 iterations using strong Wolfe line search, history size 30, `tolerance_grad` = 10^{-10} , and `tolerance_change` = 10^{-12} ; the loss weights are $(w_{\text{pde}}, w_L, w_R, w_B, w_T) = (1, 1, 1, 1, 10)$. For Stage B, we use Adam with learning rate 10^{-3} for 10,000 iterations with mini-batches of size 4096 for interior points, 1024 for the initial condition, and 1024 for the inlet condition, followed by full-batch L-BFGS for 2,000 iterations with the same settings; the loss weights are $(w_{\text{pde}}^{(c)}, w_{\text{ic}}, w_{\text{in}}) = (1, 0.01, 10)$. For the multiscale cases, both Stage A and Stage B use 50,000 Adam iterations followed by 20,000 L-BFGS iterations.

CRedit author statement

Yuhe Wang: Conceptualization, Methodology, Software, Validation, Formal analysis, Investigation, Visualization, Writing - Original Draft, Review & Editing. **Min Wang:** Conceptualization, Methodology, Formal analysis, Investigation, Writing - Review & Editing.

Data and Code Availability

The code and data used in this study are available in the GitHub repository <https://github.com/neural-basis-method/nbm>

References

- [1] Olav Møyner. Multiscale simulation of flow and transport in porous media. *Collections*, 52(08), 2019.

- [2] Eliyahu M Farber, Nicola M Seraphim, Kesha Tamakuwala, Andreas Stein, Maja Rücker, and David Eisenberg. Porous materials: The next frontier in energy technologies. *Science*, 390(6772):eadn9391, 2025.
- [3] Juan Alcalde, Stephanie Flude, Mark Wilkinson, Gareth Johnson, Katriona Edlmann, Clare E Bond, Vivian Scott, Stuart MV Gilfillan, Xènia Ogaya, and R Stuart Haszeldine. Estimating geological co2 storage security to deliver on climate mitigation. *Nature communications*, 9(1):2201, 2018.
- [4] Samuel Krevor, Heleen De Coninck, Sarah E Gasda, Navraj Singh Ghaleigh, Vincent de Gooyert, Hadi Hajibeygi, Ruben Juanes, Jerome Neufeld, Jennifer J Roberts, and Floris Swennen-huis. Subsurface carbon dioxide and hydrogen storage for a sustainable energy future. *Nature Reviews Earth & Environment*, 4(2):102–118, 2023.
- [5] Allen G Hunt and Muhammad Sahimi. Flow, transport, and reaction in porous media: Percolation scaling, critical-path analysis, and effective medium approximation. *Reviews of Geophysics*, 55(4):993–1078, 2017.
- [6] Eric Vanden-Eijnden. Heterogeneous multiscale methods: a review. *Communications in Computational Physics* 2 (3), pages 367–450, 2007.
- [7] George Em Karniadakis, Ioannis G Kevrekidis, Lu Lu, Paris Perdikaris, Sifan Wang, and Liu Yang. Physics-informed machine learning. *Nature Reviews Physics*, 3(6):422–440, 2021.
- [8] Maziar Raissi, Paris Perdikaris, and George E Karniadakis. Physics-informed neural networks: A deep learning framework for solving forward and inverse problems involving nonlinear partial differential equations. *Journal of Computational physics*, 378:686–707, 2019.
- [9] Sifan Wang, Shyam Sankaran, Hanwen Wang, and Paris Perdikaris. An expert’s guide to training physics-informed neural networks (2023). *Preprint at <https://arxiv.org/pdf/2308.08468.pdf>*, 2023.
- [10] Sifan Wang, Yujun Teng, and Paris Perdikaris. Understanding and mitigating gradient flow pathologies in physics-informed neural networks. *SIAM Journal on Scientific Computing*, 43(5):A3055–A3081, 2021.
- [11] Rafael Bischof and Michael A Kraus. Multi-objective loss balancing for physics-informed deep learning. *Computer Methods in Applied Mechanics and Engineering*, 439:117914, 2025.
- [12] Aditi Krishnapriyan, Amir Gholami, Shandian Zhe, Robert Kirby, and Michael W Mahoney. Characterizing possible failure modes in physics-informed neural networks. *Advances in neural information processing systems*, 34:26548–26560, 2021.
- [13] Chenxi Wu, Min Zhu, Qinyang Tan, Yadhu Kartha, and Lu Lu. A comprehensive study of non-adaptive and residual-based adaptive sampling for physics-informed neural networks. *Computer Methods in Applied Mechanics and Engineering*, 403:115671, 2023.
- [14] Sifan Wang, Xinling Yu, and Paris Perdikaris. When and why pinns fail to train: A neural tangent kernel perspective. *Journal of Computational Physics*, 449:110768, 2022.
- [15] Zhihang Xu, Min Wang, and Zhu Wang. Weak transnet: A petrov-galerkin based neural network method for solving elliptic pdes. *arXiv preprint arXiv:2506.14812*, 2025.

- [16] Susanne C Brenner and L Ridgway Scott. *The mathematical theory of finite element methods*. Springer, 2008.
- [17] Ivo Babuška and Werner C Rheinboldt. A-posteriori error estimates for the finite element method. *International journal for numerical methods in engineering*, 12(10):1597–1615, 1978.
- [18] George Cybenko. Approximation by superpositions of a sigmoidal function. *Mathematics of control, signals and systems*, 2(4):303–314, 1989.
- [19] Andrew R Barron. Universal approximation bounds for superpositions of a sigmoidal function. *IEEE Transactions on Information theory*, 39(3):930–945, 2002.
- [20] Dmitry Yarotsky. Error bounds for approximations with deep relu networks. *Neural networks*, 94:103–114, 2017.
- [21] Guang-Bin Huang, Qin-Yu Zhu, and Chee-Kheong Siew. Extreme learning machine: theory and applications. *Neurocomputing*, 70(1-3):489–501, 2006.
- [22] Jingrun Chen, Xurong Chi, Zhouwang Yang, et al. Bridging traditional and machine learning-based algorithms for solving pdes: the random feature method. *J Mach Learn*, 1(3):268–298, 2022.
- [23] Ali Rahimi and Benjamin Recht. Random features for large-scale kernel machines. *Advances in neural information processing systems*, 20, 2007.
- [24] Suchuan Dong and Zongwei Li. Local extreme learning machines and domain decomposition for solving linear and nonlinear partial differential equations. *Computer Methods in Applied Mechanics and Engineering*, 387:114129, 2021.
- [25] Zezhong Zhang, Feng Bao, Lili Ju, and Guannan Zhang. Transferable neural networks for partial differential equations. *Journal of Scientific Computing*, 99(1):2, 2024.
- [26] Yong Shang, Fei Wang, and Jingbo Sun. Randomized neural network with petrov–galerkin methods for solving linear and nonlinear partial differential equations. *Communications in Nonlinear Science and Numerical Simulation*, 127:107518, 2023.
- [27] Yong Shang and Fei Wang. Randomized neural networks with petrov–galerkin methods for solving linear elasticity and navier–stokes equations. *Journal of Engineering Mechanics*, 150(4):04024010, 2024.
- [28] Jingbo Sun, Suchuan Dong, and Fei Wang. Local randomized neural networks with discontinuous galerkin methods for partial differential equations. *Journal of Computational and Applied Mathematics*, 445:115830, 2024.
- [29] Xiaojun Chen, Robert S Womersley, and Jane J Ye. Minimizing the condition number of a gram matrix. *SIAM Journal on optimization*, 21(1):127–148, 2011.
- [30] Shijun Zhang, Hongkai Zhao, Yimin Zhong, and Haomin Zhou. Fourier multi-component and multi-layer neural networks: Unlocking high-frequency potential. *arXiv preprint arXiv:2502.18959*, 2025.
- [31] Jan Willem van Beek, Victorita Dolean, and Ben Moseley. Local feature filtering for scalable and well-conditioned domain-decomposed random feature methods. *Computer Methods in Applied Mechanics and Engineering*, 449:118583, 2026.

- [32] Jingrun Chen and Longze Tan. High-precision randomized iterative methods for the random feature method. *arXiv preprint arXiv:2409.15818*, 2024.
- [33] Xinwei Hu, Jingrun Chen, and Haijun Yu. A morphology-adaptive random feature method for inverse source problem of the helmholtz equation. *arXiv preprint arXiv:2510.09213*, 2025.
- [34] Shijun Zhang, Hongkai Zhao, Yimin Zhong, and Haomin Zhou. Why shallow networks struggle to approximate and learn high frequencies. *Information and Inference: A Journal of the IMA*, 14(3):iaaf022, 2025.
- [35] Xurong Chi, Jingrun Chen, and Zhouwang Yang. The random feature method for solving interface problems. *Computer Methods in Applied Mechanics and Engineering*, 420:116719, 2024.
- [36] P.B. Bochev and M.D. Gunzburger. *Least-Squares Finite Element Methods*. Applied Mathematical Sciences. Springer New York, 2009.
- [37] Gerhard Starke. Multilevel boundary functionals for least-squares mixed finite element methods. *SIAM journal on numerical analysis*, 36(4):1065–1077, 1999.
- [38] Zhiqiang Cai, R Lazarov, Thomas A Manteuffel, and Stephen F McCormick. First-order system least squares for second-order partial differential equations: Part i. *SIAM Journal on Numerical Analysis*, 31(6):1785–1799, 1994.
- [39] Zhiqiang Cai, Thomas A Manteuffel, and Stephen F McCormick. First-order system least squares for second-order partial differential equations: Part ii. *SIAM Journal on Numerical Analysis*, 34(2):425–454, 1997.
- [40] Leszek Demkowicz and Jayadeep Gopalakrishnan. A class of discontinuous petrov–galerkin methods. part i: The transport equation. *Computer Methods in Applied Mechanics and Engineering*, 199(23-24):1558–1572, 2010.
- [41] Leszek Demkowicz and Jay Gopalakrishnan. A class of discontinuous petrov–galerkin methods. ii. optimal test functions. *Numerical Methods for Partial Differential Equations*, 27(1):70–105, 2011.
- [42] Lu Lu, Pengzhan Jin, Guofei Pang, Zhongqiang Zhang, and George Em Karniadakis. Learning nonlinear operators via deepnet based on the universal approximation theorem of operators. *Nature machine intelligence*, 3(3):218–229, 2021.
- [43] Sifan Wang, Hanwen Wang, and Paris Perdikaris. Learning the solution operator of parametric partial differential equations with physics-informed deepnets. *Science advances*, 7(40):eabi8605, 2021.
- [44] Nikola Kovachki, Zongyi Li, Burigede Liu, Kamyar Azizzadenesheli, Kaushik Bhattacharya, Andrew Stuart, and Anima Anandkumar. Neural operator: Learning maps between function spaces with applications to pdes. *Journal of Machine Learning Research*, 24(89):1–97, 2023.
- [45] Martin A Grepl and Anthony T Patera. A posteriori error bounds for reduced-basis approximations of parametrized parabolic partial differential equations. *ESAIM: Mathematical Modelling and Numerical Analysis*, 39(1):157–181, 2005.

- [46] Yuan Qiu, Wolfgang Dahmen, and Peng Chen. Variationally correct operator learning: Reduced basis neural operator with a posteriori error estimation. *arXiv preprint arXiv:2512.21319*, 2025.
- [47] Kaiming He, Xiangyu Zhang, Shaoqing Ren, and Jian Sun. Deep residual learning for image recognition. In *Proceedings of the IEEE conference on computer vision and pattern recognition*, pages 770–778, 2016.
- [48] James C Robinson, José L Rodrigo, and Witold Sadowski. *The three-dimensional Navier–Stokes equations: Classical theory*, volume 157. Cambridge university press, 2016.
- [49] Junping Wang, Yanqiu Wang, and Xiu Ye. A robust numerical method for stokes equations based on divergence-free h (div) finite element methods. *SIAM Journal on Scientific Computing*, 31(4):2784–2802, 2009.
- [50] Alfio Quarteroni, Andrea Manzoni, and Federico Negri. *Reduced basis methods for partial differential equations: an introduction*, volume 92. Springer, 2015.
- [51] GR Gavalas, PC Shah, and John H Seinfeld. Reservoir history matching by bayesian estimation. *Society of Petroleum Engineers Journal*, 16(06):337–350, 1976.
- [52] Dean S Oliver and Yan Chen. Recent progress on reservoir history matching: a review. *Computational Geosciences*, 15(1):185–221, 2011.
- [53] Gregor Gantner and Rob Stevenson. Further results on a space-time fossils formulation of parabolic pdes. *ESAIM: Mathematical Modelling and Numerical Analysis*, 55(1):283–299, 2021.
- [54] Franck Boyer. Analysis of the upwind finite volume method for general initial-and boundary-value transport problems. *IMA Journal of Numerical Analysis*, 32(4):1404–1439, 2012.
- [55] Timothy Barth, Raphaèle Herbin, and Mario Ohlberger. *Finite Volume Methods: Foundation and Analysis*, pages 1–60. John Wiley & Sons, Ltd, 2017.
- [56] Leszek Demkowicz and Jay Gopalakrishnan. The discontinuous petrov–galerkin method. *Acta Numerica*, 34:293–384, 2025.
- [57] David Gottlieb and Chi-Wang Shu. On the gibbs phenomenon and its resolution. *SIAM review*, 39(4):644–668, 1997.
- [58] Anthony T Patera. A spectral element method for fluid dynamics: laminar flow in a channel expansion. *Journal of computational Physics*, 54(3):468–488, 1984.
- [59] Leszek Demkowicz, Jay Gopalakrishnan, and Antti H Niemi. A class of discontinuous petrov–galerkin methods. part iii: Adaptivity. *Applied numerical mathematics*, 62(4):396–427, 2012.
- [60] Zezhong Zhang, Feng Bao, Lili Ju, and Guannan Zhang. Transnet: Transferable neural networks for partial differential equations. *arXiv preprint arXiv:2301.11701*, 2023.